Effect of climate change at least as large as El Niño in strengthening Hurricane Polo

Authors

Ben Clarke, *Centre for Environmental Policy, Imperial College, London, UK*
Theodore Keeping, *Centre for Environmental Policy, Imperial College, London, UK*
Daniel Gilford, *Climate Central, Princeton, NJ, USA*
Kristina Dahl, *Climate Central, Princeton, NJ, USA*
Ruth Cerezo-Mota, *Laboratorio de Ingeniería y Procesos Costeros, Unidad Académica Sisal del Instituto de Ingeniería de la UNAM, Sisal, Mexico*
Clair Barnes, *Centre for Environmental Policy, Imperial College, London, UK*
Izidine Pinto, *Royal Netherlands Meteorological Institute (KNMI), De Bilt, The Netherlands*
Karina Izquierdo Rodríguez**,** *Red Cross Red Crescent Climate Centre, The Hague, the Netherlands (based in Mexico City, Mexico)*
Wenchang Yang, *Department of Geosciences, Princeton University, Princeton, NJ 08544, USA*
Friederike Otto, *Centre for Environmental Policy, Imperial College, London, UK*

Review authors

Sjoukje Philip, *Royal Netherlands Meteorological Institute (KNMI), De Bilt, The Netherlands*
Claire Bergin, *ICARUS Climate Research Centre, Maynooth University, Maynooth, Ireland*
Arunima Cheruvathoor, *Centre for Environmental Policy, Imperial College, London, UK*
Roop Singh, *Red Cross Red Crescent Climate Centre, The Hague, The Netherlands (based in New Jersey, USA)*

Cite as Clarke, B. et al. (2026): Effect of climate change at least as large as El Niño in strengthening Hurricane Polo (WWA Scientific Report No. 93). DOI: 10.25560/144926

Main findings

- Hurricane Polo first made landfall as a Category 2 storm in a sparsely populated region of Baja California Sur, with fishing communities and inland villages, limiting exposure of people and infrastructure to hurricane-force winds and storm surge. By its second landfall, east of Guaymas, it had weakened to a Category 1 hurricane. Impacts were comparatively limited, with early evacuation, shelters, pre-positioned response capacity, community preparedness, and coordination across the three levels of government helping to reduce losses.

- The rainfall associated with Hurricane Polo in north-western Mexico is a common event in today's climate, with similar rainfall totals expected approximately every two years in which there is a similar El Niño. The potential intensity conditions were less common, with a return period of around five years in today's climate in such an El Niño state.

- To estimate if human-induced climate change influenced the heavy rainfall, we first determine if there is a trend in the observations. Observation-based datasets suggested that over the historical record, such rainfall extremes have become substantially more likely and intense as the world has warmed. Overall, the observations suggest that events like the rainfall from Hurricane Polo in the study region have become about 6 times as likely and, equivalently, such 1-in-2 year events have become about 57% wetter, albeit with very large uncertainties on these estimates. This is an extremely large increase, beyond what would be expected from the effect of a warmer atmosphere holding additional moisture. This could be due to other amplifying feedbacks with warming and dynamical shifts in rainfall patterns, but may also relate to weaknesses in the available datasets or a strong role of internal variability. Further work is required to understand all of the drivers of this trend.

- The historical observations suggested a minor connection with the concurrent ENSO conditions, with an increase in likelihood of a factor of about 1.1 to 1.4 and in intensity around 3 to 15%.

- To determine the role of climate change in the rainfall, we combine observations with climate models. We find that climate models are not able to represent the observed trends and many underestimate the extreme rainfall. This is a known problem in the region. Thus, we cannot quantify the role of climate change in the rainfall, but we highlight that the increasing trend in observations is what is expected in a warming climate according to the underlying physics.

- In addition to rainfall, we analyse the very warm sea surface temperatures (SSTs) over which Polo passed before reaching peak intensity were around 1.4°C hotter than in a preindustrial climate, or equivalently it was around 200 times as likely for such elevated SSTs to occur in this region.

- The sea surface and atmospheric conditions leading to a storm's intensity were also studied using a metric known as *potential intensity.* We find that models and observations strongly agree on increases due to human-induced climate change, though observations give a much stronger trend to date. Synthesising both data sources we find that such conditions have become significantly more likely at around a factor of 23, which would make it a 1 in 115

year event without human-induced climate change. Equivalently, the potential intensity became roughly 5 m/s stronger.

- We find that the influence of El Niño is very strong, although smaller than the influence of climate change. Compared to neutral conditions, under the current July-September El Niño, the PI in September 2026 was around 14 times more likely. This suggests that it would be a 1 in 70 year event even in the present climate with neutral conditions. Equivalently, the potential intensity was roughly 4.2 m/s stronger.

- Using a complementary method to estimate the potential intensity, we also found that, the potential intensity along Polo's intensifying track was approximately 4.4 m/s higher than climatology, and the actual peak wind speed of the storm was approximately 2.7 m/s higher than it would have been without human induced climate change.

- Polo left behind property damage in the Baja Peninsula and Sonora, and flooding in coastal and low-lying areas. Landslides blocked roads at several points of the federal highway showing that the impacts of a hurricane can extend far beyond its path and continue even as the storm weakens. Heavy rainfall caused flooding and mudslides in inland and dry areas, affecting communities far from where the hurricane made landfall. This highlights the importance of preparing not only for strong winds near the coast, but also for flooding and other hazards that can affect distant communities as the storm moves.

- Although early warnings and preparation helped limit Hurricane Polo's impacts, luck also played a role, as it weakened before landfall and mainly affected sparsely populated areas. Hurricane Otis, which struck Acapulco in 2023 and caused an estimated $16 billion in damage, illustrates how impacts depend not only on storm intensity but also on where hurricanes make landfall. As the climate warms, increasingly intense hurricanes threaten more populated areas, underscoring the need for adaptation and disaster preparedness.

1 Introduction

Developing as a tropical depression on the 20th of September, Hurricane Polo intensified rapidly to a hurricane in 24 hrs. By Tuesday the 22nd at 6 am the National Hurricane Centre (NHC) upgraded the system to Category 5 on the Saffir-Simpson scale, having been classified as a tropical storm only a day before (Copernicus, 2026). This extremely rapid intensification was considered one of the fastest ever observed in the eastern Pacific, with the storm strengthening as it moved over exceptionally warm ocean waters that provided large amounts of heat and moisture to the developing system (NASA, 2026). Following this dramatic increase in strength, Polo stalled for several days, fluctuating between Category 5 and Category 4 intensity (NASA, 2026a). This prolonged period over warm waters allowed the hurricane to maintain access to substantial amounts of moisture and energy, conditions that have been exacerbated by the El Niño-Southern Oscillation (ENSO) with larger-than-normal positive anomalies of sea surface temperature (SST), potentially increasing the severity of the eventual impacts. However, the slow movement of the storm also provided residents with additional time to prepare, including boarding up homes, securing property and seeking shelter before the hurricane reached land (BBC, 2026). Polo eventually made landfall in Baja California Sur, Mexico, on the 28th of September, having weakened considerably to a Category 2 hurricane by the time it reached the coast. Despite its reduced wind intensity, the storm continued to pose significant

hazards, particularly through heavy rainfall, flooding and strong winds. After crossing the Baja California peninsula, Polo made a second landfall on the Mexican mainland, east of Guaymas, on the 29th of September, as a Category 1 hurricane (ABC News, 2026).

The storm caused widespread disruption across parts of Baja California Sur and Sonora, with coastal villages particularly affected by flooding and damage caused by fallen trees and strong winds (PBS, 2026). Although the direct damage in Baja California Sur was described as relatively limited, Polo's impacts extended beyond the immediate areas where it made landfall. After crossing the Gulf of California and reaching Sonora, the weakening hurricane continued to produce heavy rainfall and strong winds, with authorities warning of further flooding and mudslides. The National Hurricane Center forecast 4–6 inches (100–150 mm) of rainfall across southern and central Sonora, with isolated areas potentially receiving up to 8 inches (200 mm) (Reuters, 2026). Despite severe damage to infrastructure and some local communities experiencing blackouts, Polo affected relatively sparsely populated regions. Additionally, the early warnings and additional preparation time appear to have helped reduce potential loss of life. As of the latest reports, no fatalities have been recorded as a result of Hurricane Polo in Baja California Sur (Reuters, 2026), but four were killed in floods in Jalisco (The Rio Times, 2026) and one in Sonora (Diario de Yucatan, 2026).

The remnants of Hurricane Polo also brought heavy rain and flooding to a swath of the United States. As of the writing of this report, the country did not suffer any reported deaths, though flash flooding across parts of the Southwest and Midwest regions led to hazardous conditions and substantial damage: vehicles became stranded in floodwaters; drivers of stranded vehicles required helicopter rescues; homes flooded; and roadways across several states were affected by both floodwaters and debris that crews spent days clearing (abc10, 2026; The Weather Channel, 2026). In New Mexico, roughly 1,000 people residing in small towns had to evacuate their homes due to concerns over the potential failure of a dam (CNN, 2026).

Figure 1 shows the synoptic evolution of precipitation and the mid-tropospheric circulation between the 27th of September and the 2nd of October 2026. On the 27th of September, Hurricane Polo is visible as a pronounced, closed circulation over the subtropical eastern Pacific, approaching the western coast of Mexico. The hurricane subsequently made landfall in Baja California Sur on the 28th of September as a Category 2 system, before making a second landfall near Guaymas, Sonora, as a weakening but still dangerous storm (AccuWeather, 2026). The system brought heavy rainfall to parts of northwestern Mexico, with locally accumulated precipitation exceeding 4 inches (100 mm). By the 30th of September, Polo dissipated over northwestern Mexico.

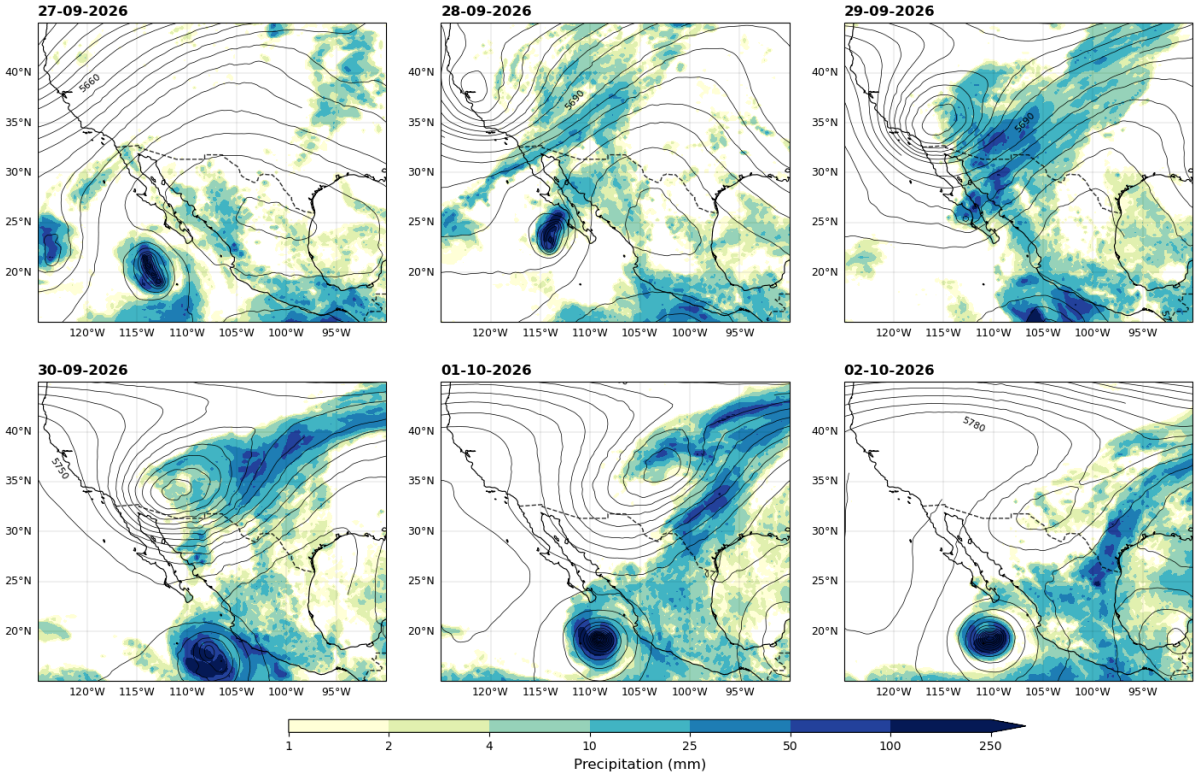

Figure 1.1: *Daily rainfall and 500 hPa geopotential height (z500) between 27 September - 2 October 2026. Data: ERA5 analysis.*

1.1 Hurricanes and heavy rainfall in the eastern Pacific

Hurricane season over the Pacific runs from June to November. In the eastern Pacific, the 2026 season was forecast to be above normal (CPC, 2026) due to the strong influence of the rising El Nino. When it formed in mid-September, Polo was the 17th tropical system with a name and the 6th major category (NHC, Eastern Pacific 2026), and the 3rd one to make landfall on the Mexican coast this season. It was also the 2nd most intense hurricane recorded in the eastern Pacific after 2015 Hurricane Patricia (that happened during another intense ENSO year.).

There are few studies on the influence of climate change on tropical cyclones in the eastern Pacific. The extremely active season of 2015 in the eastern and central Pacific was found to be driven primarily by warming in the subtropical Pacific Ocean related to anthropogenic forcings rather than the influence of El Nino (Murakami et al., 2017). In 2023, Hurricane Otis rapidly intensified off the Mexican coast and made landfall as a Category 5, bringing heavy rainfall and extreme winds speeds to the densely populated, becoming the costliest hurricane in Mexican history (Garcia-Franco et al., 2024). While no specific attribution study has been conducted for this storm, its rapid intensification coincided with a period of unusually high sea surface temperatures (Garcia-Franco et al., 2024) related to a marine heatwave (Radfar et al., 2024). While the rise in marine heatwaves and elevated SSTs is robustly linked to anthropogenic warming globally (e.g. Giguere et al., 2024; Laufkotter et al., 2024), the implications of this, along with other factors affecting the development and intensification of TCs, remain understudied in this region.

Heavy rainfall in northwestern Mexico is driven by a range of phenomena throughout the year. The North American Monsoon is active from mid-June to mid-September, with a region of high pressure dominating over the southwestern US and southerly winds bringing moisture from the Gulf of California and tropical Pacific. From June-November, tropical cyclones and mesoscale convective systems also bring periodic extreme rainfall, while throughout the winter extreme rainfall is dominated by extra-tropical cyclones, frontal systems and atmospheric rivers (Vega-Camarena et al., 2024).

1.2 Event Definition

In this study, we characterise Hurricane Polo in several ways in order to capture both the environmental conditions that drove its intensity and the range of ways the associated extreme rainfall and high winds led to impacts. This study follows the same methodology as recent rapid studies on Typhoon Gaemi (World Weather Attribution, 2024a), and Hurricanes Helene (World Weather Attribution, 2024b) and Melissa (World Weather Attribution, 2025). The report is broken into three sections.

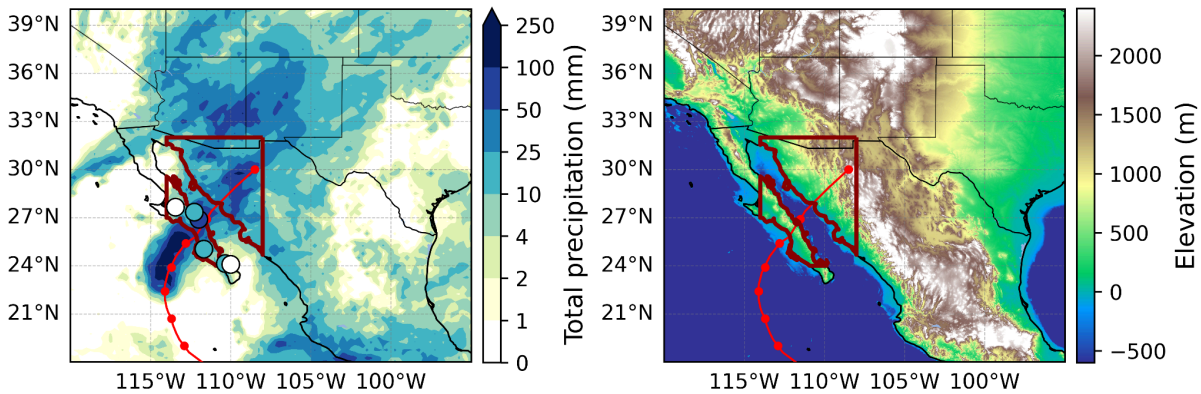

Figure 1.2: *Left: Total precipitation on 28-29th September 2026 including ERA5 data and local weather stations. Right: Elevation across Mexico and the southern US. On both panels, the study region is outlined in dark red and the track of Hurricane Polo is shown in red.*

First, the WWA protocol is applied to extreme rainfall across the landfall region in which impacts were reported and which has a broadly consistent elevation and climatology, covering part of the states of Baja California Sur and Sonora in Mexico, and extending slightly into the southern US (Fig. 1.2). The choice of season is discussed in section 2. This analysis gives a probabilistic analysis of precipitation extremes using a synthesis of observational and climate model products. The rainfall event definition is as follows:

- ***Landfall region (Rx1dayTC):*** *September-November maximum 1-day accumulations over land areas within the region 24-32°N and 114-108°W (figure 1.2)*

Second, we characterise the conditions that led to such an event, using two different approaches. The potential intensity (PI) is a metric that predicts maximum typhoon wind speed using sea surface temperatures, sea level pressure, and temperature and humidity vertical profiles (Pérez-Alarcón et al., 2023; Emanuel, 1986; Gilford 2020). The PI during the month of September is analysed in section 3

using the WWA method. The PI and sea surface temperatures (SSTs) are also studied in isolation in section 4, using Climate Central's Climate Shift Index: Ocean systems. While PI and SSTs are related, studying SSTs in isolation helps to disentangle the influence of climate change on the more complex overall PI quantity. We also use the Climate Shift Index: Tropical Cyclones system to quantify the change in Polo's lifetime maximum intensity (LMI) attributable to human-caused climate change. Using a combination of different approaches, as we have done here, increases our confidence in the final resultant statement.

Environmental conditions:

- ***Potential Intensity (section 3):*** *September mean of monthly mean PI averaged over ocean areas bounded by 120 - 100°W, 10 - 30°N (Fig. 1.3)*
- ***Sea Surface Temperatures (section 4):*** *Along Hurricane Polo's track and a bounded track region, 110–95°W, 5–20°N (Fig. 1.3)*
- ***Potential Intensity (section 4):*** *Along Hurricane Polo's track*
- ***Lifetime Maximum Intensity (section 4):*** *Wind speed at the point of first Lifetime Maximum Intensity*

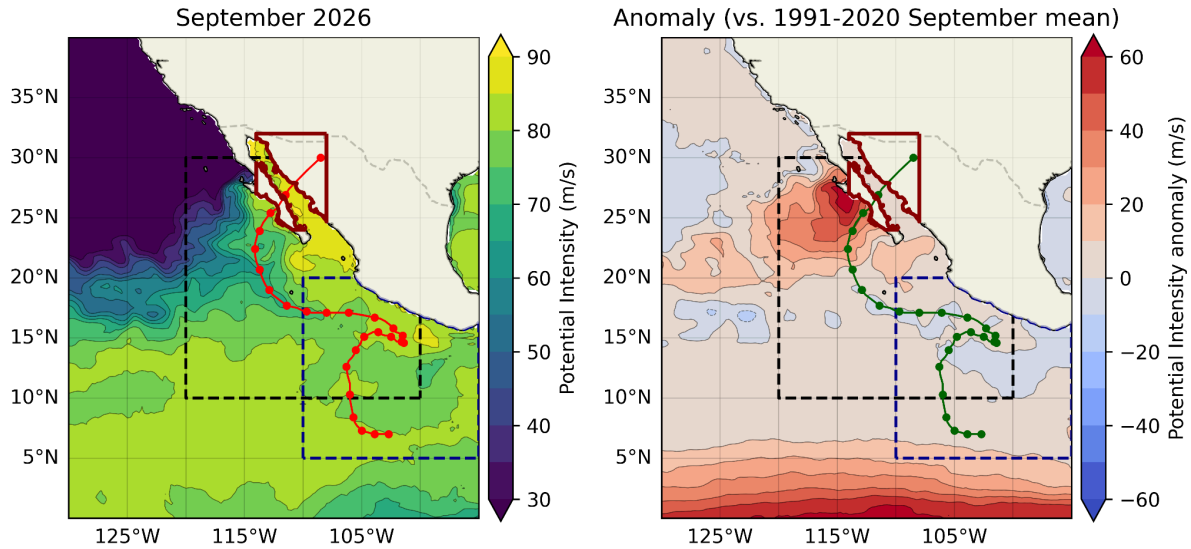

Figure 1.3: *September mean potential intensity in the eastern Pacific region (left) and the anomaly of these monthly values with respect to the 1991-2020 climatology of September mean potential intensity (right). The study region is highlighted with the dashed black line and the track of Hurricane Polo is shown as red (left) and dark green (right) points. The black dashed box shows the track region analysed by WWA (section 3) while the blue box indicates the region analyzed by Climate Central (section 4). Data from ERA5.*

For each event definition, we study the influence of anthropogenic climate change by comparing the likelihood and intensity of similar extremes at present with those in a 1.4°C cooler climate (1.3°C in section 4) without human-caused warming (based on Forster et al., 2026). For the rainfall and potential intensity in sections 2 and 3 we also extend this analysis into the future by assessing the influence of a further 1.4°C of global warming from present. This is in line with the latest Emissions

Gap Report from the United Nations Environment Programme, which shows that the world is on track for at least 2.8°C temperature rise given currently implemented policies (UNEP, 2025).

2. Extreme rainfall attribution using WWA protocol

2.1 Observational analysis

2.1.1 Season selection

To determine the appropriate seasonality to capture the extreme rainfall from Hurricane Polo, we considered several factors. The eastern Pacific hurricane season stretches from 15th May to 30th November. Western Mexico also experiences a summer monsoon from June to September, which results in a large fraction of the annual rainfall (between 60 to 80%). This is evident from the seasonal cycles of daily mean rainfall over the study region, with the climatological rain (Fig 2.1). The seasonal cycles also highlight that the majority of rainfall extremes fall from September through the winter. We therefore hypothesized that restricting the event definition from September, when the event occurred and the monsoon ends, to November, to coincide with the end of the tropical cyclone season, would characterize this event more effectively than a longer season.

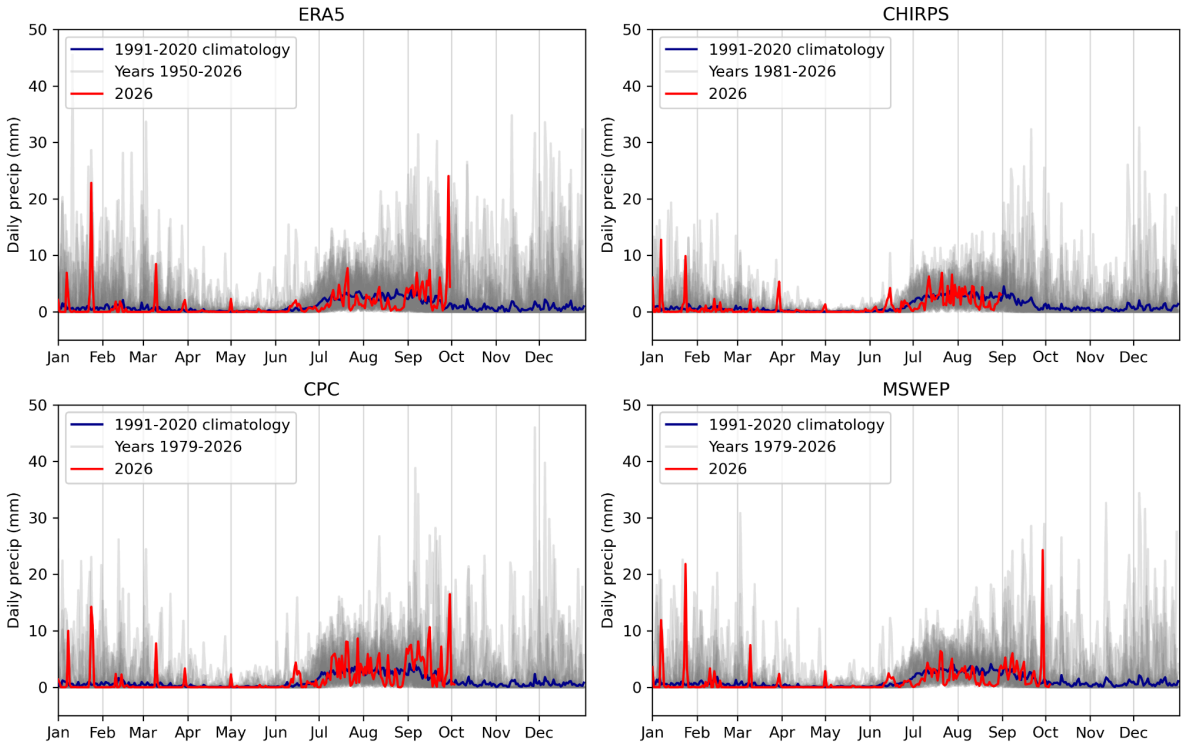

Figure 2.1: *Historical record of daily rainfall averaged over the study region in four observational and reanalysis datasets: ERA5, CHIRPS, CPC and MSWEP. 2026 values are shown as a red line, the 1991-2020 climatology in dark blue, and all other years are shown in grey.*

We tested the seasonal choice by comparing the dates of seasonal maxima from both June-November and September-November to nearby tropical cyclones from the historical record according to

IBTrACS (see section A.1.1.1 for details). For each dataset, we checked whether a TC passed within a region 5° beyond the study region on all sides, and within two days either side of the resultant seasonal maxima. Time series and detected nearby TC events are shown for September-November in Fig. 2.2. The results showed a consistently higher fraction of the historical maxima were associated with TCs in September-November (ERA5: 66.2%, CPC: 77.1%, CHIRPS: 73.3%) than in June-November (ERA5: 59.7%, CPC: 64.6%, CHIRPS: 60.9%). We also assessed linear trends in the wettest day of the respective season at each grid cell, finding that the trends were overall slightly weaker in September-November, but broadly consistent spatially (see Fig. A.2.1). Furthermore, we are confident that our results are dominated by changes in tropical cyclone-associated rainfall extremes.

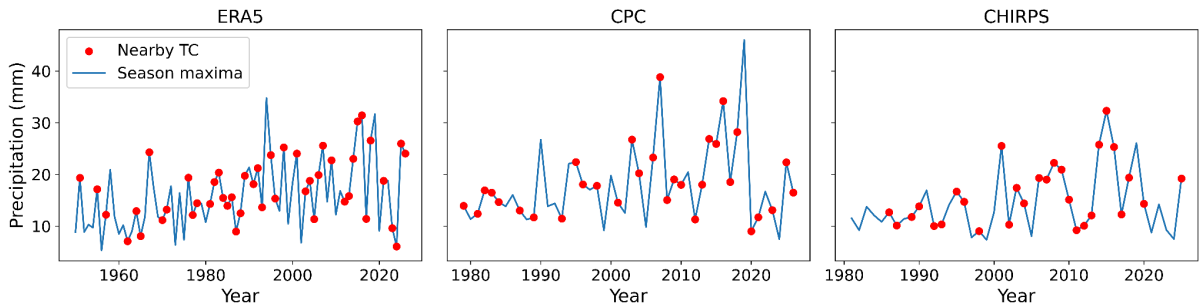

Figure 2.2: *Time series of September-November maximum 1-day rainfall averaged over the study region in ERA5 (left), CPC (middle) and CHIRPS (right). Red dots indicate a nearby tropical cyclone passage according to IBTrACS.*

2.1.2 Trend analysis

The event definition studied in this section is the September-November maximum 1-day precipitation accumulation over land areas within the region 24-32°N and 114-108°W (Fig. 1.2) - referred to as Rx1dayTC. The methods used to analyse rainfall trends follow the standard WWA protocol using non-stationary extreme value theory, as described in Philip et al. 2020 and expanded upon in Otto et al., 2024. Specifically, the extremes index Rx1dayTC is calculated from each dataset and is modelled using a generalised extreme value (GEV) distribution that is assumed to scale with global mean surface temperature (see Appendix A1 for details of data and methods). In line with the protocol described in Philip et al. 2020, climate models are evaluated in their representation of observed weather and climate characteristics of the region (see Appendix A.3).

The El Niño - Southern Oscillation (ENSO) is known to influence the occurrence rate and intensity of tropical cyclones in this region at certain times of the year (section 1.1). Therefore, we first investigate the effect of including ENSO as an additional covariate in the statistical model (section A.1.1.3) represented by the relative Niño3.4 index, averaged over the July-September period to capture the conditions immediately preceding and concurrent with this event. It is worthy of note that this covariate does not sufficiently improve the fit, according to the Akaike information criterion, with respect to a statistical model using GMST as the sole covariate. This may be due to a lag in the onset of its influence in the region (Hausfather, 2026). We therefore do not consider ENSO throughout our analysis. However, we assess its influence in the observational datasets to quantify the extent to which it may have influenced this event relative to the influence of warming in the historical record.

The return period estimates in observation-based datasets with the event included suggest that the conditions observed in September 2026 are now relatively common in the present climate, with such accumulations expected approximately once every 2 years given such ENSO conditions (Table 2.1). These estimates are consistent across the two datasets, ERA5 and CPC, that include the event, with substantially overlapping 95% confidence intervals. We further note that the choice of return period affects the estimated probability ratios but that the estimated changes in intensity are independent of the return period. The results for the change in characteristics of such extremes with human-caused climate change and with ENSO conditions in each of the observational datasets are also shown in Table 2.1, with both probability ratios for events of equivalent intensity, and changes in intensity of an event of equivalent likelihood. All results are discussed in detail below.

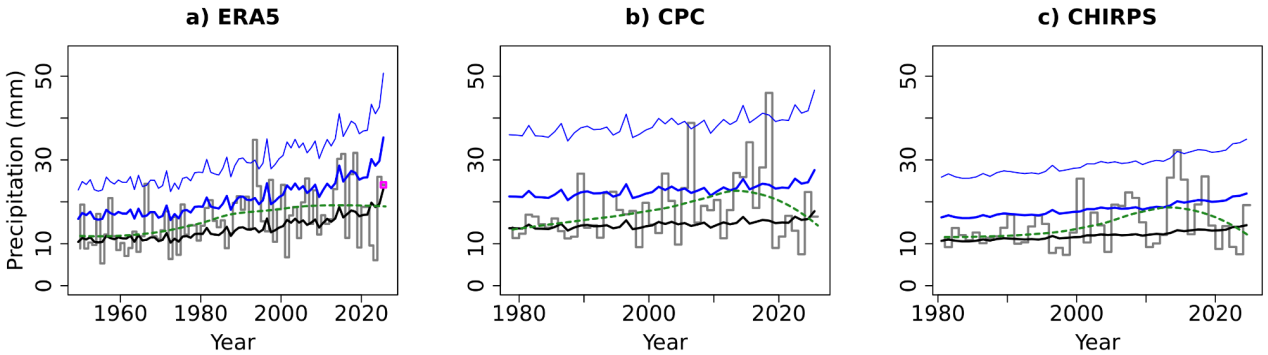

Figure 2.3: *Time series of Rx1dayTC in the landfall study region for three observation-based datasets. The loess smoothed trend is shown with the dashed green line, while the expected values and 1-in-5 and 1-in-50 years return period events each year from the fitted statistical model including GMST and July-September ENSO as covariates are shown with the black, thick blue and thinner blue lines, respectively.*

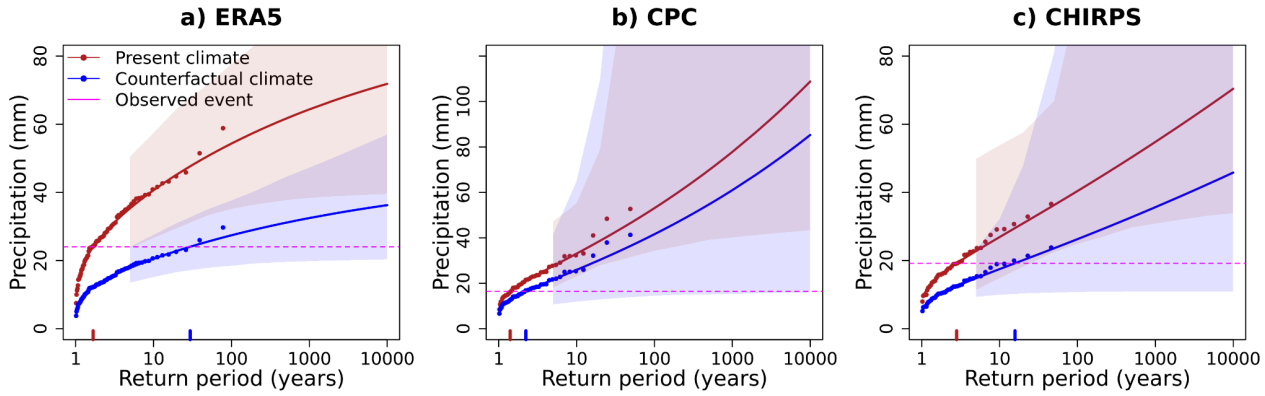

Figure 2.4: *Return curves for Rx1dayTC in the landfall study region for three observation-based datasets. The event magnitude (2-year return period event for CHIRPS) is shown with the dashed pink line. The red line shows the best fit curve to the data scaled to the present climate, while the blue curve shows the data scaled to the preindustrial climate for a model including both GMST and ENSO, assuming the ENSO value of 2026. Shaded areas show the 95% confidence interval obtained through bootstrapping.*

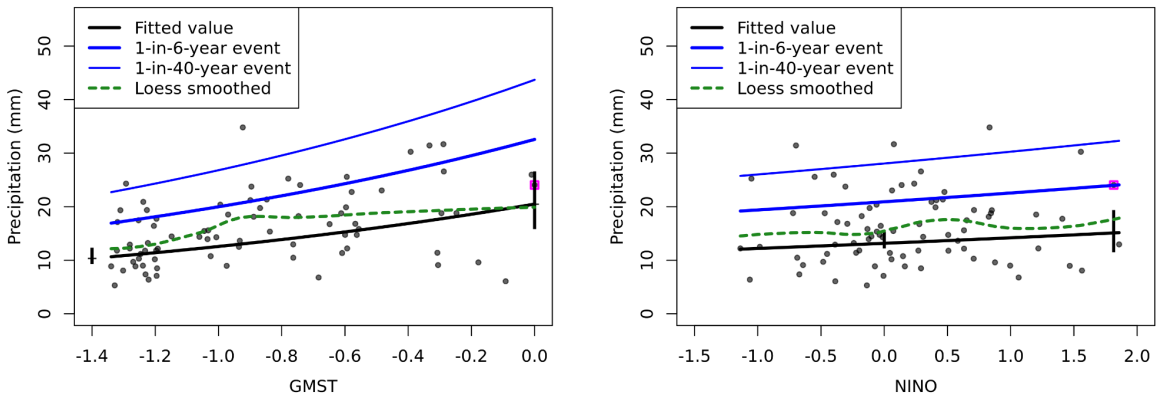

Figure 2.5: *Rx1dayTC in the landfall study region against covariates GMST (left) and ENSO (right) in the ERA5 dataset. The Loess smoothed trend is shown with the dashed green line, while the expected values and 1-in-6 and 1-in-40 years return period events each year from the fitted statistical model are shown with the black, thick blue and thinner blue lines, respectively.*

Figure 2.3 and 2.4 show the statistical model fit to each dataset. The loess smoothed trend in all time series shows a generally increasing trend over time, with a small dip in recent years in the shorter datasets CPC and CHIRPS that is not captured by the GEV model. It is also clear that the addition of the ENSO covariate does not fully capture the variability in the time series, as the time series remain substantially more variable than the expected value year-by-year (Fig. 2.3). However, all models exhibit a broadly increasing trend and are broadly well represented by the GEV model at all except the rarest events in CPC (Fig. 2.4).

Results are also broadly consistent across datasets for both covariates, albeit with substantial quantitative variation and large uncertainties. Compared to a neutral ENSO year, the analysis suggests that current El Niño resulted in a small increase (Fig. 2.5): by a factor of approximately 1.1-1.4 in PR and 3-15% in intensity (Table 3.1). All datasets indicate a larger increase in likelihood and intensity due to global warming. CPC and CHIRPS both indicate changes in likelihood of approximately 2-4, with a wider uncertainty range of ~0.3 to infinity. The longest dataset, ERA5, shows a statistically significant increase of a factor of 33 (3.5 to infinity). The change in rainfall intensity is similarly variable, with estimates from 28% in CPC to 98% in ERA5, and all estimates far above Clausius-Clapeyron scaling suggestive of some combination of super-Clausius-Clapeyron scaling, a substantial dynamical shift, weakness in the available datasets, or a strong role of internal variability beyond ENSO. Uncertainties for individual datasets are very large and we have not been able to access long-term station data records, suggesting that model analysis is also needed to refine this estimate. This finding is in line with another study, finding strong and statistically significant observed trends in heavy precipitation in the region in September-November (and June-August) (Dai et al., 2025).

Dataset	Event		Influence of 1.4°C GMST increase		Influence of El Niño	
	Magnitude (mm)	Return period	Probability ratio	Change in rainfall	Probability ratio	Change in rainfall

				intensity (%)		intensity (%)
ERA5	24.1 26.4	1.68 (1.14, 5.44) 2	**17.6** **(2.80, >1m)** **33.4** **(3.55, >1m)**	**98.1** **(31.6, 175)**	1.32 (0.675, 2.34) 1.42 (0.610, 2.88)	14.7 (-11.2, 51.6)
CPC	16.5	1.41 (1.02, 3.88) 2	1.59 (0.292, >1m) 1.94 (0.263, >1m)	27.6 (-43.8, 308)	1.15 (0.780, 2.46) 1.24 (0.672, 2.50)	9.39 (-20.8, 49.5)
CHIRPS	16.8	2	4.21 (0.283, >1m)	53.7 (-40.2, 391)	1.07 (0.407, 1.71)	2.80 (-24.2, 50.2)

Table 2.1: *Return period and observed/derived magnitude for the 2026 event, as well as probability ratio and change in magnitude for the September-November maximum rainfall in the NW Mexico region due to both GMST and ENSO. For the ERA5 and CPC datasets, both the estimated return periods and the final return period (2 years), and the results using these return periods are shown, with the change in intensity consistent across return periods. Statistically significant results at the 95% level are highlighted in* ***bold text****.*

2.1.3 Circulation analogues

Atmospheric flow analogues can be used to assess changes in the intensity of dynamically similar events or changes in the frequency of occurrence of particular circulation patterns (Vautard et al., 2023; Jézéquel et al., 2018, Thompson et al 2024). Here we use ERA5 data to assess analogues identified from 500 hPa geopotential height (Z500) since 1950, to detect changes in the frequency of circulation patterns similar to those associated with the heavy rainfall event.

To identify the most similar events, we compute the Euclidean distance between the Z500 anomaly field of the 29th September 2026 and every other day (1950–2024) over the region bounded by [130° to 95°W, 15° to 45°N]. To avoid double-counting persistent events, the identified events must be separated by at least 5 days. The region and circulation variable were determined by assessing the event itself, and earlier current understanding of the circulation drivers of similar events (Holgate et al 2023).

To detect trends in the circulation pattern and intensity since 1950 we identify the closest 29 analogues across the two periods (1950-1979 and 1995-2024). This corresponds to the closest 1% of days in each period. The average weather conditions associated with the two sets of analogues - called ‘composites’ - are then compared to assess differences between the two periods. Differences in modes of internal variability between the two time periods can also induce differences in the weather conditions, therefore we cannot identify the role of climate change solely by comparing analogue sets in reanalyses.

The analogue analysis shows that, even though the composite past and present analogues for Z500 are good in terms of the large-scale circulation pattern, the corresponding composite precipitation analogues do not produce rainfall of similar magnitude and location. This may be due to the small spatial scale of the tropical system with respect to the wider circulation patterns studied. However, conducting the same analysis using sea level pressure (SLP) over a smaller domain rather than Z500 gives similar results. This makes a conditional association of the type of circulation from 29th September 2026 with rainfall not possible. Factors other than dynamics play a major role in the precipitation event here. Therefore we do not use the circulation analogue results in the synthesised findings.

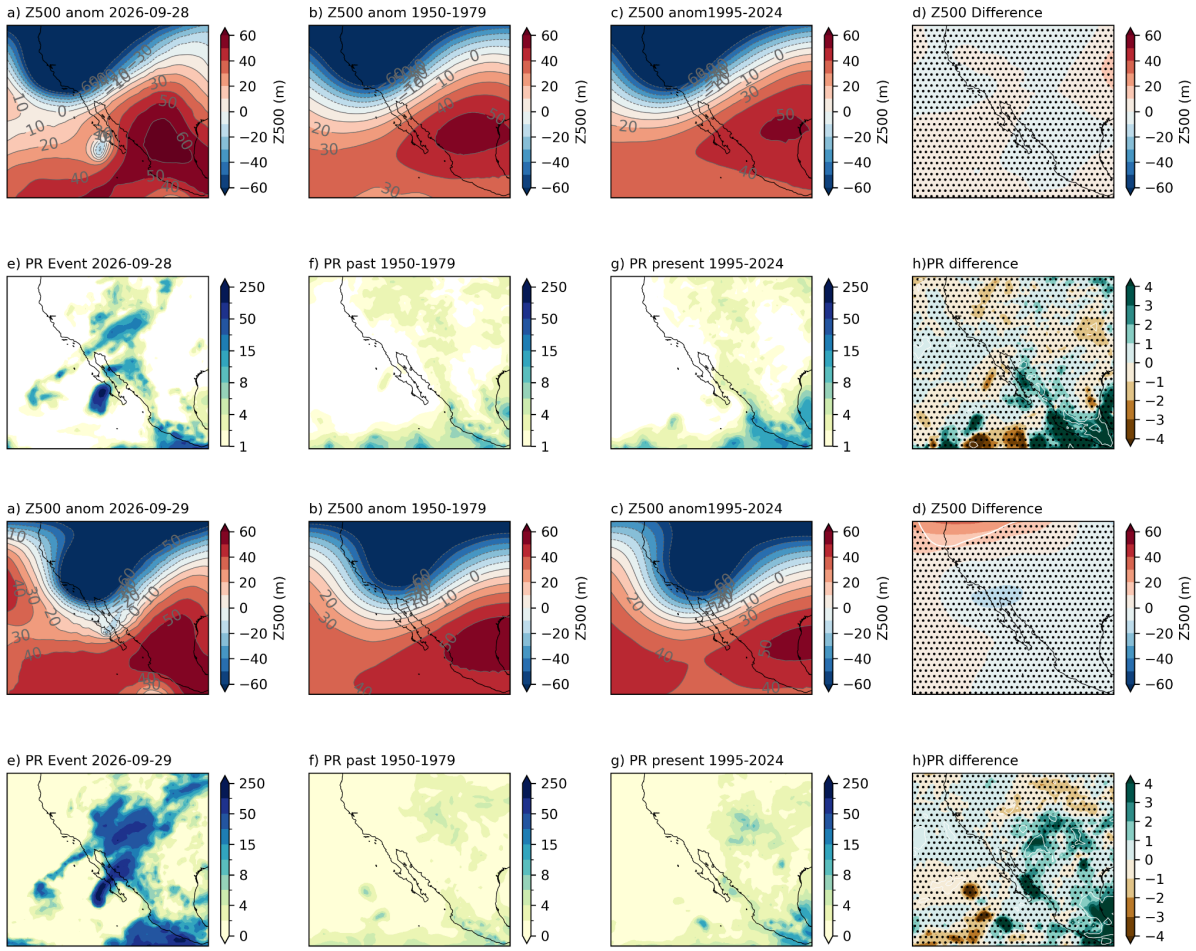

Figure 2.6: *Circulation analogue analysis for Hurricane Polo, based on 28th September (top 2 rows) and 29th September (bottom 2 rows). For each pair, the top row shows Z500 and the bottom row shows precipitation. a) and e) shows the data on 29 September 2026, b) and f) show the composite of the past, and c) and g) show the composites of the present period. d) and h) show the difference between the composites of present and past (present minus past), where dots mean the difference is not significant.*

2.2 Multi-model attribution

This section shows Probability Ratios and change in rainfall intensity ΔI for models that passed model

evaluation (see section A.3) and also includes the values calculated from the fits with observations. For the purposes of the synthesis, the analysis of observation-based datasets in section 2.1.2 is rerun using GMST as the sole covariate to match models. These statistical models are also used for model evaluation purposes. All models with more than one ensemble member (shown in brackets by the model name in the synthesis figure) are first synthesised into a single estimate before being included in the wider synthesis.

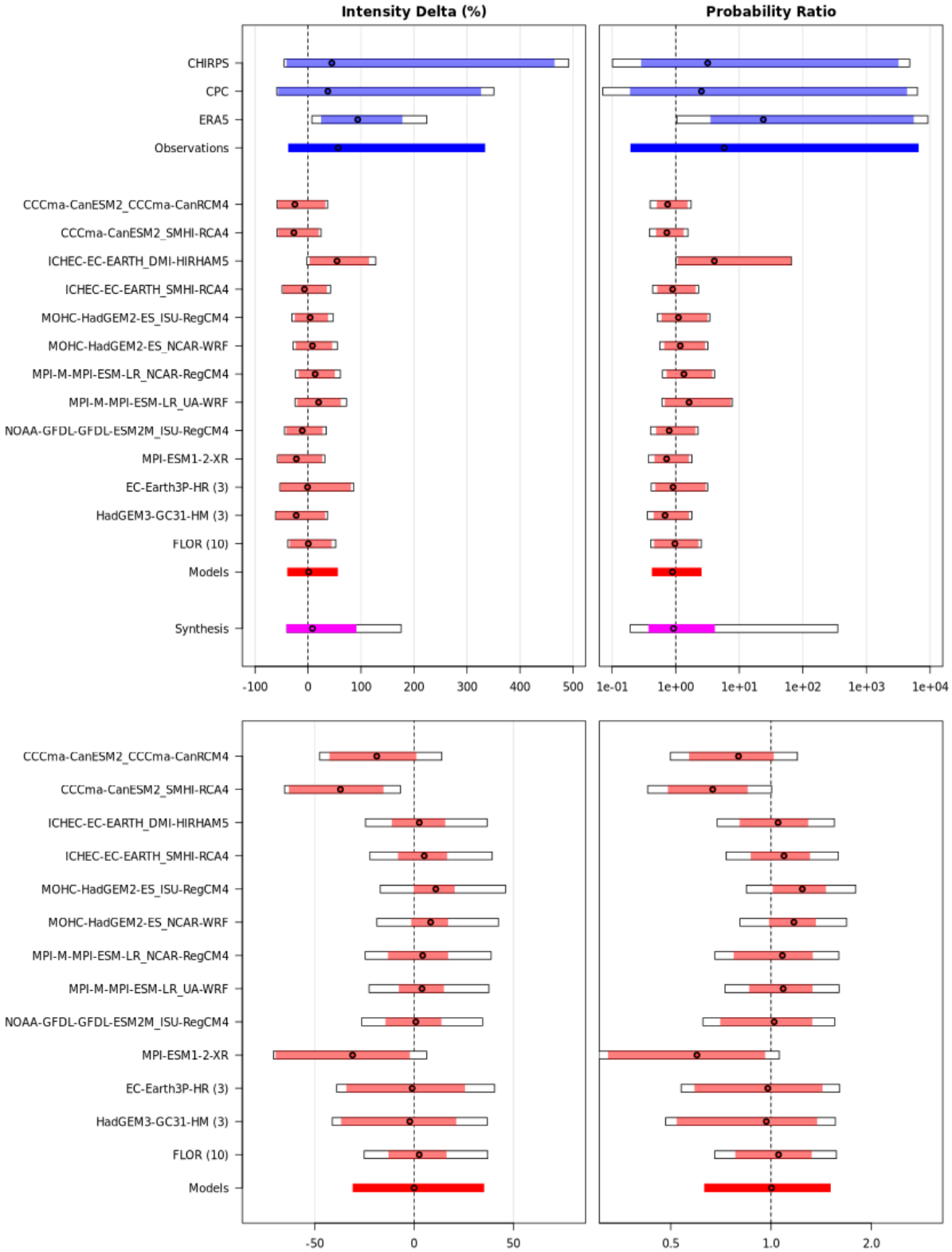

Figure 2.7: *Synthesised changes for the 2-year September-November 1-day precipitation event in the study region due to GMST. Changes in rainfall intensity (left) and PR (right) are shown for a historical period comparing the past 1.4°C cooler climate with the present (top row) and for a future period, based on model projections only, comparing the present and a 2.8 °C warmed climate (bottom row).*

3 Potential Intensity attribution using WWA protocol

3.1 Observational analysis

The event definition studied in this section is the September mean of potential intensity averaged over ocean areas within 120-100°W, 10-30°N (Fig. 1.2). As in section 2, the methods used to analyse potential intensity trends follow the standard WWA protocol using non-stationary extreme value theory, as described in Philip et al. (2020) and expanded upon in Otto et al., (2024). Specifically, the potential intensity is calculated from the ERA5 data and is modelled using a Gaussian distribution that is assumed to shift with global mean surface temperature (see Appendix A1 for details of data and methods). In line with the protocol described in Philip et al. (2020), climate models are evaluated in their representation of observed weather and climate characteristics of the region (see Appendix A.3).

As in section 2, we investigate the effect of including ENSO as an additional covariates in the statistical model (section A.1.1.3), with ENSO represented by the relative Niño3.4 index, averaged over the July-September period to capture the conditions immediately preceding and concurrent with this event. Unlike for rainfall in NW Mexico, this covariate substantially improves the fit, according to the Akaike information criterion, with respect to a statistical model using GMST as the sole covariate. We therefore do consider this throughout our analysis.

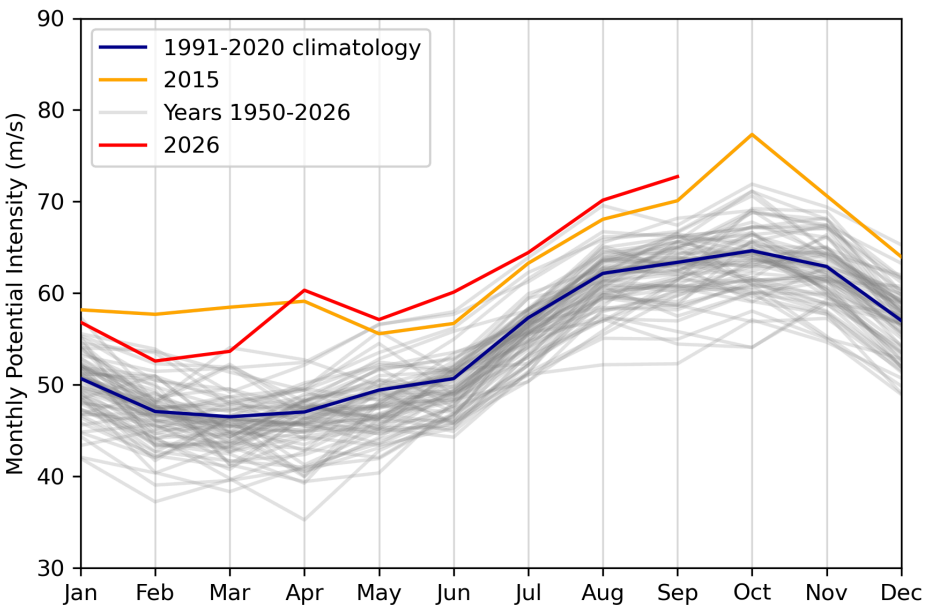

Figure 3.1: *Monthly mean potential intensity in the study region around the track of Hurricane Polo in the eastern Pacific. 2026 values are shown in red, 2015 in orange, the 1991-2020 climatological mean is shown in dark blue, and all other years in the record are shown in grey. Data: ERA5.*

The return period estimate suggests that the conditions observed in September 2026 are now relatively common in the present climate, with such values expected approximately once every 5 years given such ENSO conditions (Table 3.1). However, it is worthy of note that the potential intensity in September is the highest in the historical record for September, and is second only to October 2015, the last time ENSO values were as high as they are at present (Fig. 3.1). Indeed, the study region in the eastern Pacific has exhibited elevated potential intensity conditions for the entirety of 2026, similar to its behaviour in 2015 preceding and alongside a rising El Niño. The strong role of both El Niño and global warming are also shown by the time series (Fig. 3.2), which indicate both a long-term rise (Fig. 3.2a & b) and a degree of variability that is well captured by the ENSO index (Fig. 3.2b).

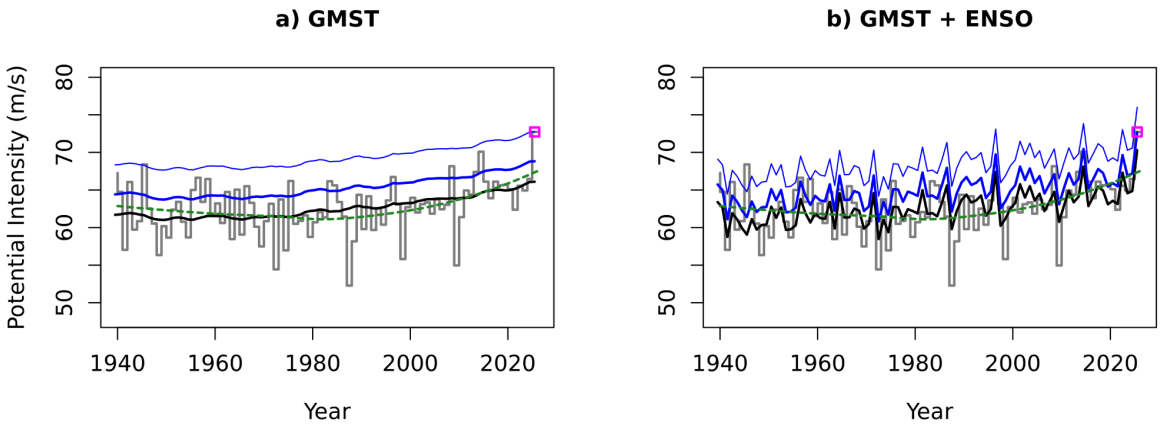

Figure 3.2: *Time series of September potential intensity in the eastern pacific study region around the track of Hurricane Polo. The loess smoothed trend is shown with the dashed green line, while the expected values and 1-in-5 and 1-in-50 years return period events each year from the fitted statistical model including GMST only (left) and GMST and July-September ENSO (right) as covariates are shown with the black, thick blue and thinner blue lines, respectively.*

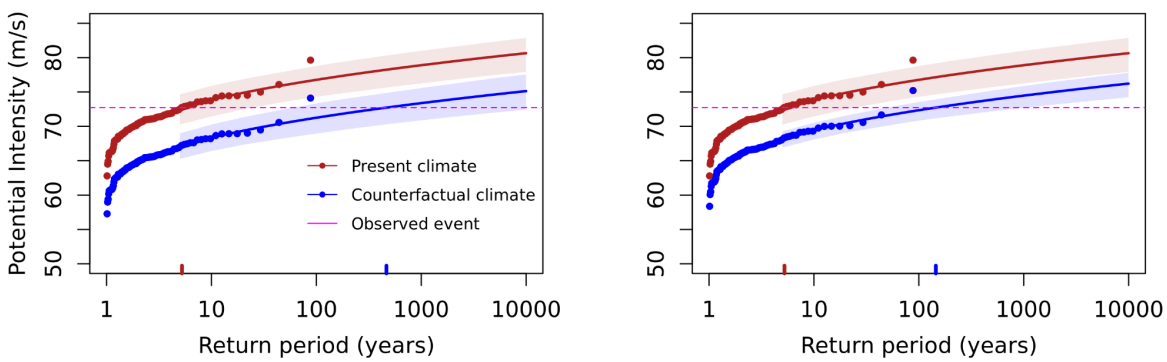

Figure 3.3: *Return curves for September PI in the eastern Pacific study region for ERA5, varying with GMST (left) and ENSO (right). The event magnitude is shown with the dashed pink line. The red line shows the best fit curve to the data shifted to the present climate conditions, while the blue curve*

shows the data scaled to the preindustrial (left) and neutral (right) climate. Shaded areas show the 95% confidence interval obtained through bootstrapping.

Dataset	Event		Influence of 1.4°C GMST increase		Influence of El Niño	
	Magnitude (m/s)	Return period	Probability ratio	Change in potential intensity (m/s)	Probability ratio	Change in potential intensity (m/s)
ERA5	72.7	5.23 (2.23, 24.3)	**89.1 (13.3, 2140)**	**5.52 (3.51, 7.41)**	**27.8 (7.45, 194)**	**4.42 (2.40, 6.35)**

Table 3.1: *Observed event magnitude, return period, probability ratio and change in magnitude for the potential intensity in September 2026 in a region around the track of Hurricane Polo, due to GMST and the current July-September El Niño. Statistically significant changes are highlighted in* ***bold text****.*

By varying the covariate GMST between its present and pre-industrial levels, and the ENSO value between current El Niño and neutral conditions, the probability ratio and change in magnitude of 2026-like events are estimated (Fig. 3.3; Table 3.1). As expected from figures 3.2 and 3.3, the PI index exhibits a strong and statistically significant increasing trend with warming. In a world that has warmed by 1.4°C, the PI in September 2026 has become around 90 (13 to 2100) times more likely, suggesting that it was previously a 1 in 450 year event even with a similar ENSO state. Equivalently, the potential intensity became roughly 5.5 (3.5 to 7.4) m/s stronger. The influence of El Niño also appears to be very strong, although smaller than the influence of climate change. Compared to neutral conditions, under the current July-September El Niño, the PI in September 2026 has become around 28 (7.5 to 190) times more likely, suggesting that it would be a 1 in 140 year event even in the present climate. Equivalently, the potential intensity became roughly 4.4 (2.4 to 6.4) m/s stronger.

3.2 Multi-model attribution

This section shows Probability Ratios and change in potential intensity ΔI for models that passed model evaluation and also includes the values calculated from the fits with observations. The synthesis process (to produce figure 3.4) is conducted as set out in section A.1.1.3. The synthesised results are also tabulated in section 6 alongside the other hazard sections for ease of comparison.

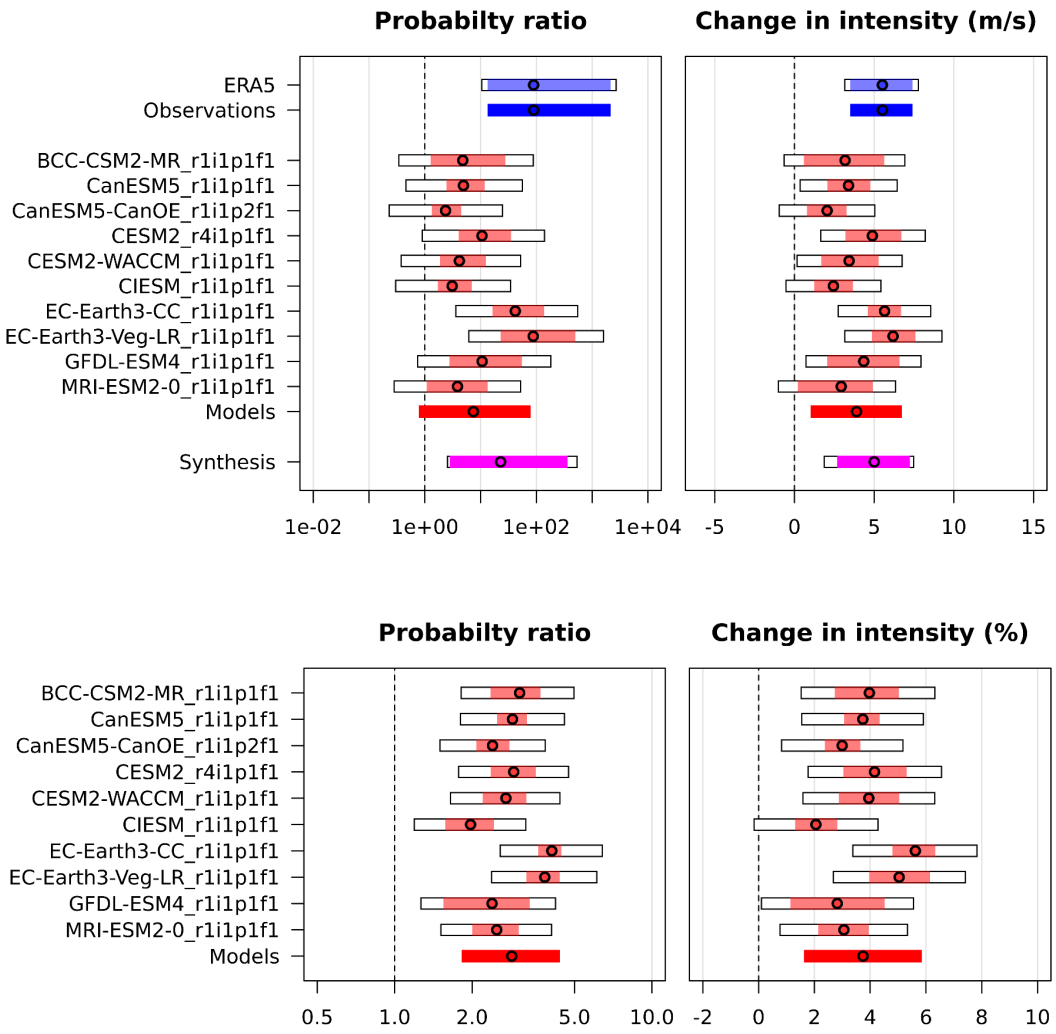

Figure 3.4: *Synthesised changes for a 5-year September mean potential intensity event in a region around the track of Hurricane Polo due to GMST. PR (left) and change in potential intensity (right) are shown for a historical period comparing the past 1.4°C cooler climate with the present (top row) and for a future period, based on model projections only, comparing the present and a 2.8 °C warmed climate (bottom row)*

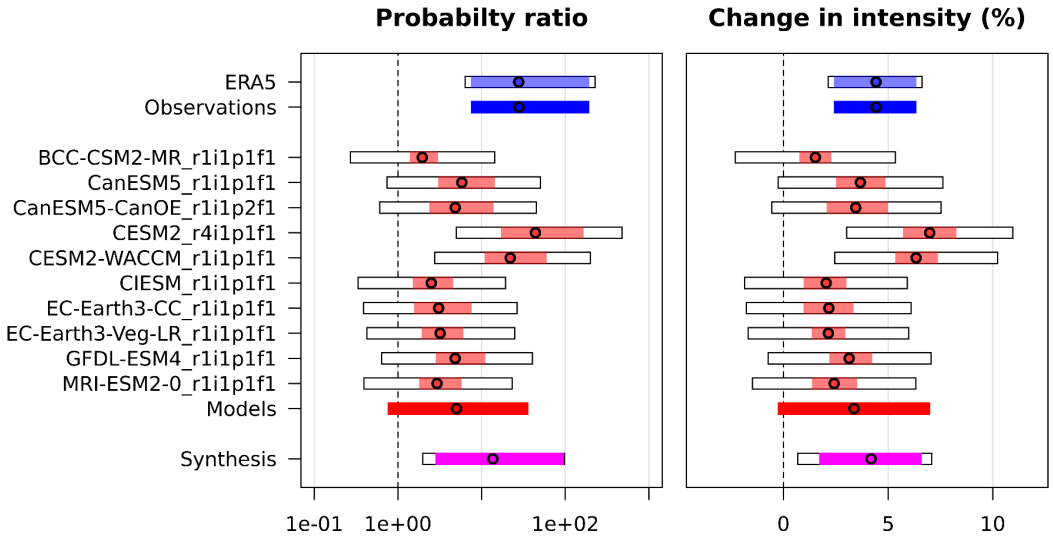

Figure 3.5: *Synthesised changes for a 5-year September mean potential intensity event in a region around EVENT track due to ENSO. PR (left) and change in potential intensity (right) are shown for a historical period comparing the past 1.4°C cooler climate with the present (top row) and for a future period, based on model projections only, comparing the present and a 2.8 °C warmed climate (bottom row)*

4 Sea Surface Temperature, Potential Intensity, and Lifetime Maximum Intensity along event track using CSI method

Climate Central's Climate Shift Index (CSI) system quantifies the contribution of climate change to daily observed sea surface temperatures (SSTs) and to hurricane wind speeds in near-real time using track and observed actual intensity values from the U.S. National Hurricane Center's operational advisory/forecast-advisory fixes. The foundations of the daily SST attribution and hurricane wind speed attribution systems were published by Giguere et al. (2024), and Gilford et al., (2024), respectively. The methodologies behind these systems are complementary to the WWA protocol in that they draw upon both empirical and climate model data to make probabilistic determinations of the changed likelihood and/or intensity of climate phenomena as a result of anthropogenic climate change.

For the purposes of this study, Climate Central calculated the influence of climate change on the likelihood and magnitude of the high SSTs Hurricane Polo encountered along its track, both up to the point of the storm's Lifetime Maximum Intensity (LMI), and as it made its way to landfall. Noting that tropical cyclones can repeatedly weaken and strengthen, the LMI in the CSI system is defined as Polo's *first* lifetime maximum wind speed. Consistent with the methods published by Gilford et al., (2024) and refined by *CSI: Tropical Cyclones*, we also calculated the attributable change in the storm's potential intensity along its track, along with the change in actual observed intensity at the LMI fix. Given that Polo's track leading up to the point at which it reached its LMI was farther south than the region in which its impacts were most acutely experienced, we focused our analysis on a slightly different region than that described above (ocean areas along Hurricane Polo's intensifying

track, bounded by 5-20°N, 110-95°W); notably, the PI variations in these regions are highly correlated (see Figure 4.3).

We note that the CSI system attributes a 1.3°C GMST increase (compared with WWA's 1.4°C GMST increase); thus the results presented here are characterized by a slightly-weaker attributable human influence. Preliminary estimates where we linearly scale-up our results to account for this 0.1°C difference results in 8% and 20% increases in attributable SST warming and PI ramping, respectively, while the attributable change in lifetime maximum wind speed remains unaffected.

4.1 Sea Surface Temperature Attribution Analysis

As Hurricane Polo traveled toward the coast of Mexico, the waters it encountered in the eastern Pacific were as warm as 31.2°C. These SSTs were 1-2°C hotter than normal (i.e., compared to a 1991-2020 average for late September). Climate Central's CSI system indicates that the SSTs Polo encountered along its track and leading up to its LMI point were about 185 times more likely (median estimate) and, on average, 1.4°C warmer than they would have been in a preindustrial world that was 1.3°C cooler globally (Fig. 4.1). Preliminary calculations updating the global mean temperature change since the preindustrial period to 1.4°C (consistent with WWA's warming level) indicate that the influence of climate change may be even larger than cited above, with an increase in likelihood exceeding 200. Note that these changed likelihood estimates are based on an occurrence ratio rather than a probability ratio, consistent with Giguere et al. (2024) and Gilford et al. (2024).

After reaching its LMI of 155 kt on the 22nd of September, Polo began moving northwestward, where it continued to encounter SSTs made significantly warmer due to climate change. In this post-LMI phase of the storm, the SSTs Polo traversed over were made about 1.1°C warmer and roughly 40 times more likely as a result of climate change (Fig. 4.2).

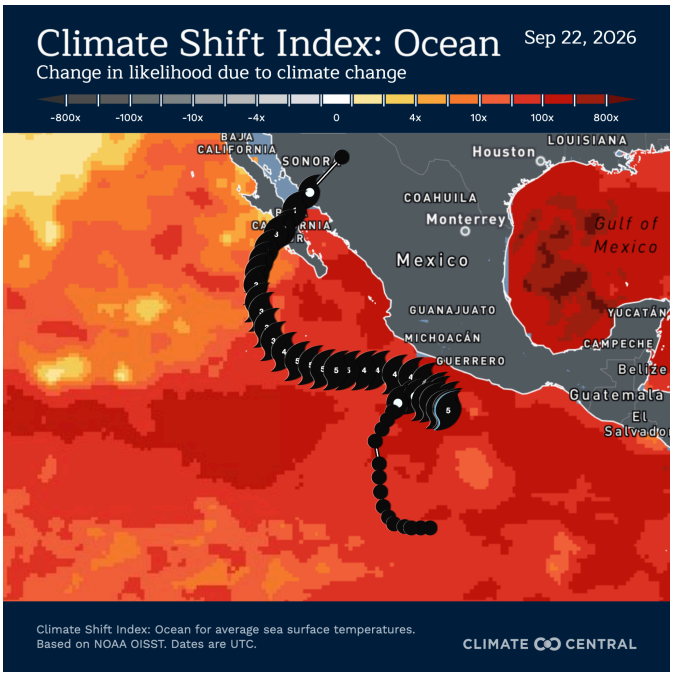

Figure 4.1: *The Climate Shift Index: Ocean values along Hurricane Polo's track indicate that the abnormally warm SSTs the storm encountered were made 185 times more likely due to human-caused*

climate change prior to its LMI, and 40 times post-LMI. Note that there is not enough reliable data in the Gulf of California to produce Climate Shift Index values. That region is therefore shown in grey.

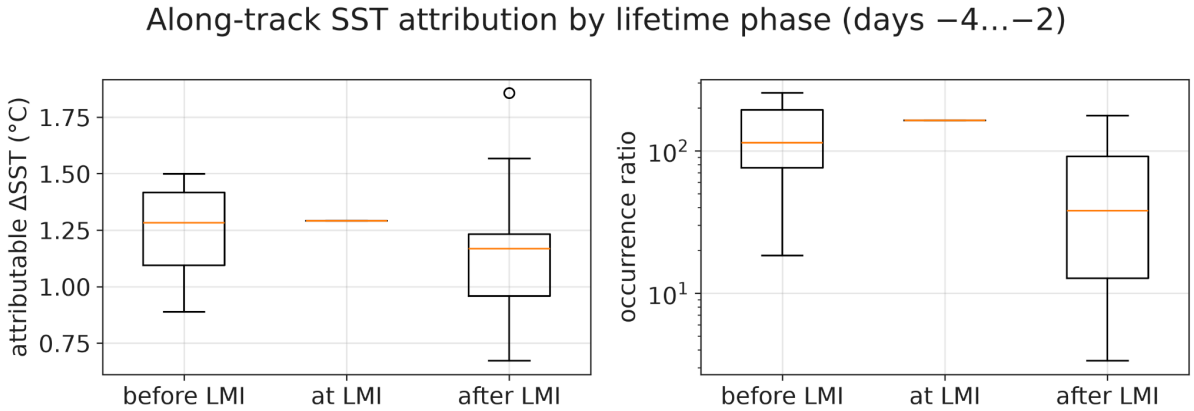

Figure 4.2: *The change in sea surface temperature (SST) attributable to climate change along Hurricane Polo's track before, at, and after the point of the storm's lifetime maximum intensity (LMI; left) as well as the occurrence ratio of the SSTs the storm encountered during each phase of its development (right).*

These anomalously warm SSTs are consistent with a long-term warming of SSTs in the region. Since the early 1980s when the world was approximately 1°C cooler, SSTs in this region have warmed by about 0.7°C due to climate change (Fig. 4.3).

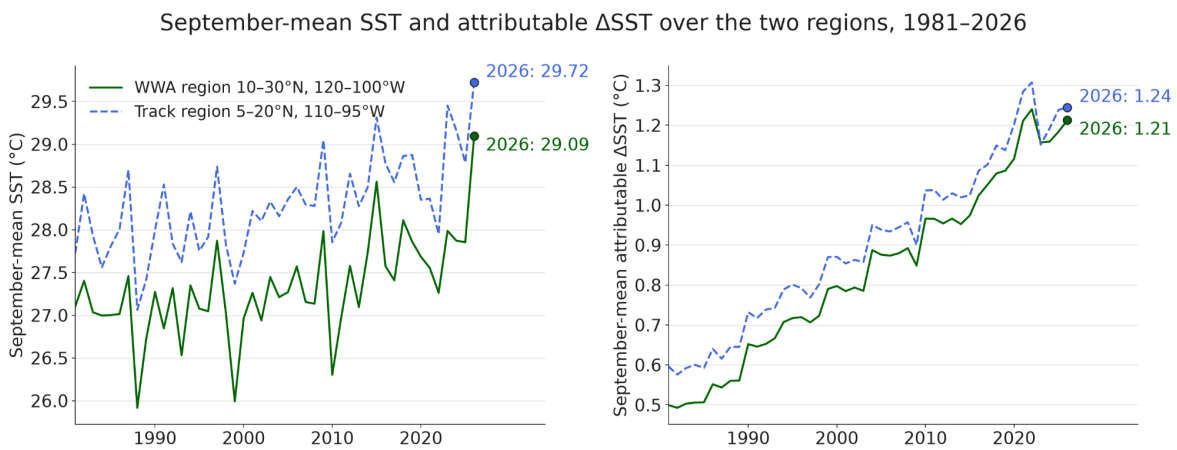

Figure 4.3: *September mean SST (left) and attributable change in SST (right) over the WWA-defined region (green) and Hurricane Polo's track region (blue dashed).*

4.2 Potential Intensity and Lifetime Maximum Intensity Attribution

The anomalously warm SSTs during this time contributed to an anomalously high potential intensity environment in which Polo developed. The potential intensity of a hurricane represents the theoretical upper limit of how strong it can become, and it is determined in part by SSTs in combination with atmospheric conditions including the temperature and humidity profiles of the atmosphere. Polo's

observed maximum intensity reached about 90% of its PI as calculated using tcpyPI v1.4 (CK/CD=0.9, dissipative heating on), making it a strong candidate for applying potential intensity theory (e.g. Gilford et al. 2019).

The potential intensity anomaly along Polo's intensifying track averaged 4.4 m/s higher than climatology, approximately 1.1 standard deviations above average before the storm's maximum intensity, and was even higher (~1.8 standard deviations above average) at its LMI and along its track through the remainder of its lifetime (Fig. 4.4). These anomalously high potential intensity values are consistent with the warmer SSTs Polo encountered as a result of climate change, though some portion of the anomalous potential intensity environment may also have been related to interannual variability, given that the storm was evolving near the the northern edge of the anomalously warm El Niño region (see section 3). Polo developed and tracked over an environment that was attributably much more conducive to higher maximum intensities (Fig. 4.5; cf. section 3). The estimated attributable change in potential intensity at Polo's LMI fix was at least 3.4 m/s higher due to climate change, and about 3.9 m/s averaged over the intensifying track.

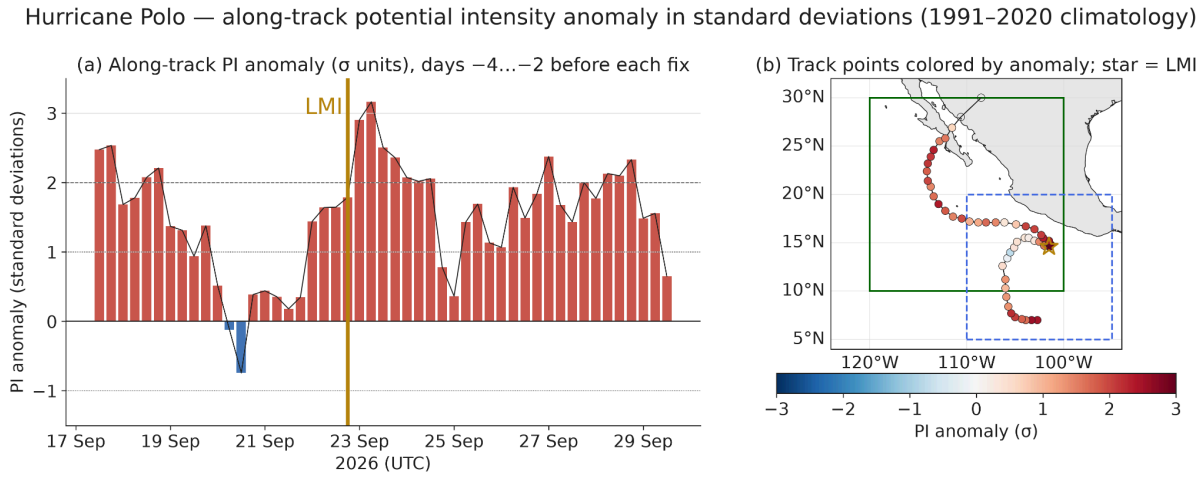

Figure 4.4: *6-hourly potential intensity anomaly (1991-2020 climatology) along Hurricane Polo's track (left). Track shaded by potential intensity anomaly (right). The storm's lifetime maximum intensity is indicated with a vertical yellow line in the left panel and a yellow star in the right. Green and blue dashed boxes represent the WWA-defined and Hurricane Polo's track regions, respectively.*

We constructed a counterfactual actual intensity at Polo's LMI based on *CSI: Tropical Cyclones*, which is based on the method of Gilford et al. (2024). This method is a potential intensity-based thermodynamic storyline attribution methodology in which shear and track are fixed. The counterfactual relies on counterfactual SSTs—taken from the CSI: Oceans system (section 4.1)—observed LMI, local environmental potential intensity, and local potential intensity sensitivity. The change in actual intensity attributable to climate change is the difference between the observed and the calculated counterfactual intensity. Using a conservative estimate that assumes a maximal damping effect of atmospheric warming on potential intensity (i.e., the damping coefficient, α, is set to -1.0, see Gilford et al. (2024)), we found that Hurricane Polo's lifetime maximum intensity was at least 2.7 m/s faster than it would have been in a world without human-caused climate change (Fig. 4.5).

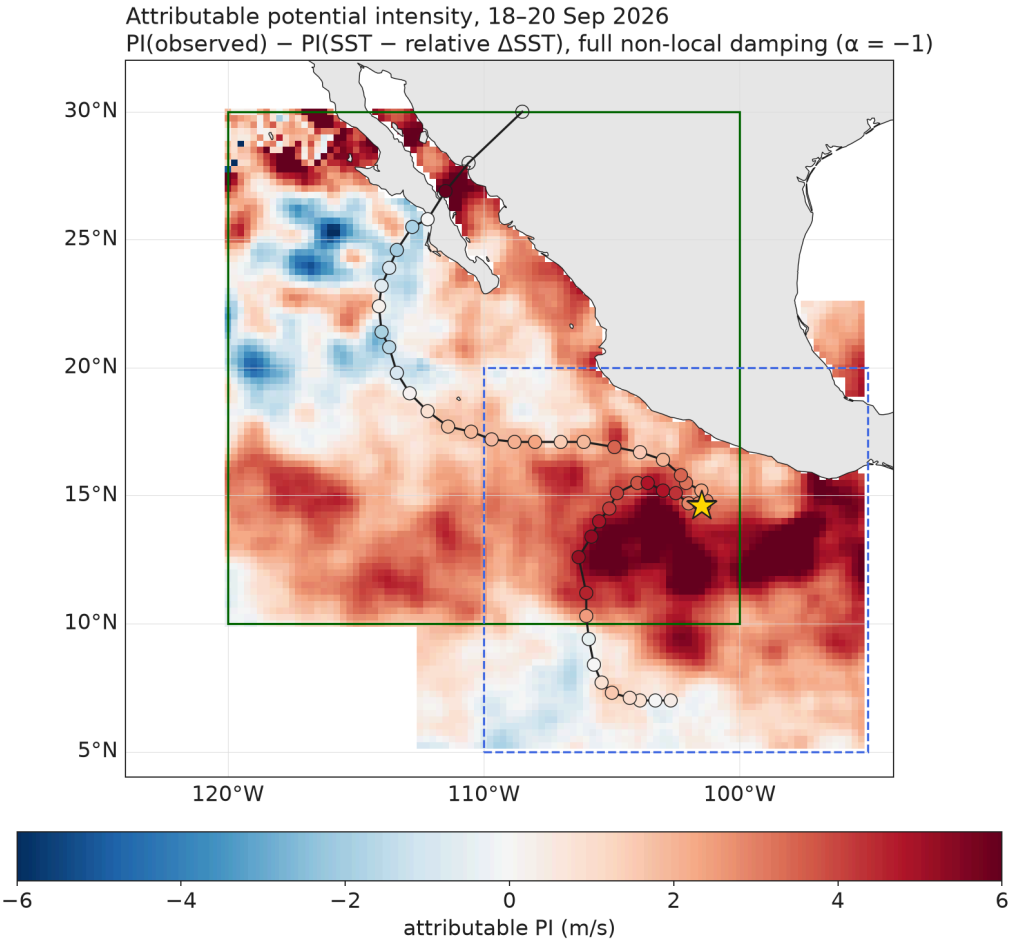

Figure 4.5: *Attributable potential intensity (m/s) along Hurricane Polo's track over September 18-20. The blue dashed box shows the track region analyzed by Climate Central while the green box indicates the region analyzed by WWA. The point of Polo's lifetime maximum intensity is shown as a yellow star.*

4.3 Interpretation of results

Hurricane intensities and rapid intensification are strongly related to elevated SSTs (e.g. Hong and Wu 2021). Increased SSTs allow for higher levels of local humidity, atmospheric instability, and potential intensity (e.g. Emanuel 2006). Along Hurricane Polo's track, ocean temperatures were consistently >1°C warmer than they would have been in a world without climate change, and were made at least 185 times more likely prior to the LMI of the storm, and about 40 times more likely during the remainder of the storm's lifetime. We conclude that warmer SSTs along the track of Hurricane Polo were strongly influenced by climate change. These climate-influenced SSTs led to an increase in the potential intensity across this region, with WWA and Climate Central's results agreeing very closely on the attributable change in potential intensity. This attributable change enabled Polo to reach a wind speed at least 2.7 m/s stronger at its LMI than what would have occurred in a world without human-caused climate change.

5 Hazard summary

This section contains all of the final results for each hazard analysis.

The return period of the rainfall from Hurricane Polo in north west Mexico was very low, with such totals expected around every other year in the present climate. Observation-based datasets suggested that over the historical record, such rainfall extremes have become substantially more likely and intense as the world has warmed. Results from the longest running observation-based dataset, ERA5, were statistically significant at the 95% level. Overall, the observations suggest that events like the rainfall from Hurricane Polo in the study region have become about 5.8 (0.23 to 5700) times as likely and, equivalently, such 1-in-2 year events have become about 57% (-29% to +330%) more intense. As discussed in section 2.1.2, this estimate is far above Clausius-Clapeyron scaling suggestive of some combination of super-Clausius-Clapeyron scaling, a substantial dynamical shift, weakness in the available datasets, or a strong role of internal variability beyond ENSO. The historical observations also suggested only a minor connection with the concurrent ENSO conditions, with an increase in likelihood of a factor of ~1.1 to 1.4 and in intensity around ~3 to 15%. This additional covariate did not improve the fit, as assessed using the akaike information criterion, compared to using GMST alone.

Observations and models disagreed that climate change from the preindustrial period to present has driven changes in likelihood and intensity of similar 1-day precipitation extremes. The climate models that passed evaluation overall estimate that events like Hurricane Polo have remained essentially unchanged, with estimates of probability ratio and change in rainfall intensity close to 1 and 0, respectively. Only a single climate model, EC-Earth HIRHAM, accurately reproduces the historical trend in the observations. This mismatch between observed and modelled trends in the region is in line with other findings in the literature (Dai et al., 2025), and is likely due in part to the inability of climate models used here to capture the complex processes involved in extreme rainfall in the study region and the influence of climate change upon these, though an influence of natural variability in historical trends and issues with gridded data products cannot be discounted. Our investigation is further hampered by a lack of long-running weather station records in the study region. On the other hand, robust thermodynamic amplification of rainfall extremes and the strong influence of environmental conditions on storms such as Polo (see below) suggest a role for climate change.

As a result of this fundamental disagreement, we calculate both the weighted synthesis, giving a greater weight to the model synthesis with lower uncertainty bounds, and the unweighted synthesis, which weights observation-based synthesis the same as the model-based estimate. The best estimates are therefore as follows. The weighted synthesis suggests that such rainfall events are essentially unchanged, with a probability ratio of 0.93 (0.44 to 3.5) and change in rainfall intensity of +8.3% (-33% to +83%). The unweighted synthesis suggests that such rainfall events have more than doubled in likelihood, with a probability ratio of 2.3 (0.22 to 310) and change in rainfall intensity of +29% (-33% to +170%). However, given the strong disagreement among lines of evidence, we conclude that while rainfall is becoming more intense in this region in the tropical cyclone season and that this is at least partially related to warming, we cannot quantify the influence of climate change. In the future at 2.8°C of warming, models project no further change again, though confidence in this finding is very low.

Changes in the potential intensity conditions forming such a storm are much clearer (Table 5.2). Using the WWA protocol, models and observations strongly agree on increases due to GMST, though

observations give a much stronger and statistically significant trend to date. Synthesising both data sources using the weighted approach, we find that such conditions have become significantly more likely at around a factor of 23 (2.8 to 360) and with a change in potential intensity of 5.0 (2.7 to 7.2) m/s. In a world that warms by a further 1.4°C, models project a further intensification of such extreme conditions by a factor of 2.9 (1.8 to 4.4) in likelihood, or equivalently 3.7 (1.6 to 5.9) m/s in intensity. Climate Central's potential intensity results agree well with those developed with the WWA protocol. The Climate Shift Index: Ocean data indicates that SSTs prior to the first LMI were about 1.4°C warmer and 185 times more likely as a result of human-caused climate change. These warm SSTs led to an average potential intensity change of about 3.9 m/s along Polo's intensifying track, with the observed lifetime maximum intensity estimated to be at least 2.7 m/s stronger as a result of climate change.

Data	**Period**	**Influence of GMST increase of 1.4°C**	
		Probability ratio (95% CI)	**Intensity change (%) (95% CI)**
Observations	**Past - present**	5.78 (0.227, 5650)	56.8 (-29.3, 326)
Models		0.890 (0.494, 2.19)	1.25 (-31.1, 48.1)
Synthesis (Weighted)		0.926 (0.438, 3.53)	8.30 (-32.5, 83.1)
Synthesis (Unweighted)		2.27 (0.222, 308)	29.0 (-32.6, 168)
Models only	**Present future**	1.00 (0.649, 1.47)	0.0452 (-28.7, 33.1)

Table 5.1: *Summary of results for Rx1dayTC, presented in Fig 2.7: changes due to GMST include past-present changes and present-future changes.*

Data	**Influence of GMST increase of 1.4°C**			**Influence of El Niño**	
	Time period	**Probability ratio (95% CI)**	**Intensity change (m/s) (95% CI)**	**Probability ratio (95% CI)**	**Intensity change (m/s) (95% CI)**
Observations	**Preindustrial - present**	**89.1 (13.3, 2140)**	**5.52 (3.51, 7.41)**	**27.8 (7.45, 194)**	**4.42 (2.40, 6.35)**
Models		7.43 (0.785, 78.9)	**3.89 (1.01, 6.74)**	5.00 (0.755, 36.3)	3.36 (-0.271, 7.01)
Synthesis		**22.9 (2.80, 361)**	**5.00 (2.68, 7.24)**	**13.6 (2.81, 96.8)**	**4.18 (1.70, 6.61)**
Models	**Present - future**	**2.85 (1.82, 4.39)**	**3.74 (1.62, 5.85)**		

Table 5.2: *Summary of results for September PI, presented in figs 3.4 & 3.5: changes due to GMST include past-present changes and present-future changes. Statistically significant changes in probability and intensity are highlighted with* ***bold text****.*

6 Vulnerability and exposure

Hurricane Polo was an unusually intense and long-lived eastern Pacific hurricane, reaching Category 5 strength twice between 23 and 26 September, with maximum sustained winds of approximately 280 km/h (NASA, 2026). After several days offshore, Polo weakened before making landfall just south of Las Barrancas, Baja California Sur, around midnight on 28 September as a Category 2 hurricane, bringing strong winds and heavy rain, before crossing the Gulf of California and making a second landfall around midday near Guaymas, Sonora, on 29 September as a Category 1 hurricane, with winds of approximately 120 km/h (Kothari, 2026).

6.1 Historical events

Although four fatalities were reported in Talpa de Allende, Jalisco, following heavy rain and flooding associated with Polo before its landfall, no fatalities were reported in Baja California Sur following the landfall (G. Partida et al., 2026), with one in Sonora following the second landfall (Diario de Yucatan, 2026). Impacts in Baja California Sur were comparatively limited, primarily involving localised flooding, road inundation, fallen trees and minor infrastructure damage (Government of Mexico, 2026). This contrasts sharply with past hurricanes such as, Hurricane Otis (2023), which made a Category 5 landfall directly over Acapulco and caused an estimated US$12–16 billion in damage, equivalent to approximately 1% of Mexico's GDP, as well as extensive destruction of homes and critical infrastructure (NOAA/NHC, 2024). A more similar comparison is Hurricane Patricia (2015), another exceptionally intense Category 5 hurricane that weakened before landfall and impacted a relatively sparsely populated area. Patricia caused severe localised damage but resulted in comparatively limited national losses, illustrating how exposure and preparedness can substantially influence outcomes even when hazard intensity is extreme (NOAA/NHC, 2016).

6.2 Storm surge

Storm surge was a major anticipated hazard for Polo, with warnings indicating that significant coastal flooding could occur as strong winds pushed water toward the shore, compounded by large, destructive waves (Hauari; NHC 2026). However, the extent of surge-related damage may have been moderated by Polo's weakening prior to landfall and the relatively small population of the immediate landfall area (AFP, 2026). Polo made landfall near las Barrancas, a coastal community of 539 inhabitants and 188 dwellings, whereas its second landfall occurred near Guaymas, a municipality with 156,863 residents (Redacción N+, 2026). This contrasts with larger urban centres, where comparable hazard intensity could expose substantially more people and assets. Although Polo had weakened to Category 2 by its second landfall, flooding was reported in parts of Guaymas, illustrating how impacts depend not only on storm intensity but also on local exposure and conditions (AP, 2026). Overall, Polo demonstrates that extreme hurricane intensity does not automatically translate into extreme losses: the location and timing of landfall, storm intensity at landfall, exposure, vulnerability and preparedness are critical determinants of the eventual impacts.

Although Polo downgraded from a hurricane to a tropical storm over northwest Mexico, its moisture still contributed to heavy rainfall inland (NHC, 2026). Flash floods and mudslides continued to pose significant dangers even as the hurricane downgraded. As of 30 September, roughly 100 million people from Arizona to Iowa were considered at risk of flash flooding from the remnants of Polo, with flood watches extending more than 1,200 miles across the southern and midwest of the U.S. (Breen, 2026). The weather service warned that the combination of saturated ground and additional heavy rain could produce dangerous flash flooding, particularly in areas affected by wildfires (Frank, 2026).

6.3 Economic capacity and livelihoods

There are notable disparities in economic capacities and livelihood dependencies across the territories along Polo's pathway. Baja California Sur, preliminary assessments reported damage to coastal fishing and aquaculture communities, tourism-based settlements, and rural farms (IERT, 2026). Coastal areas like San Carlos and Adolfo Lopez Mateos, which have modest housing made from concrete blocks or wood with tin roofs, depend mainly on tourism and fishing industries (DW, 2026). For smaller and more livelihood-dependent communities, even relatively localised physical damage can translate into prolonged income losses and reduced household capacity to recover. By contrast, larger urban economies have more diversified economic bases and institutional resources.

6.4 Spatial planning and exposure

As Hurricane Polo progressed from Baja California Sur through Sonora and towards the United States, it encountered diverse settlement patterns and populations. Along the Pacific coast of Mexico, the hurricane affected low-lying coastal settlements, while further inland its rainfall interacted with agricultural areas, rural settlements and established drainage systems. Authorities had already identified 100 communities and 65 specific points at risk of flooding across 25 coastal municipalities, demonstrating that significant portions of the exposed territory had known flood susceptibility (Government of Mexico SSPC, 2026).

The Municipal Urban Development Programme for Guaymas, for example, identifies several flood-prone areas associated with natural floodplains and drainage channels, including rural settlements and neighbourhoods within the city, and recognises that modifications to natural drainage patterns can contribute to flood hazard (SEDATU, 2024). At the same time, planning and land-management measures can reduce risk when they incorporate these hazard conditions.

The transition into the United States presents a markedly different spatial and ecological context as the Hurricane moved towards the arid and semi-arid landscapes of the Southwest, with a different form of flood risk (Breen, 2026). For example, dry arroyos, washes and desert rivers can rapidly fill during intense rainfall, concentrating water and producing flash flooding in and around settlements that may not ordinarily experience sustained surface water (IPR, 2026). Planning frameworks in places such as Maricopa County explicitly recognise this risk by implementing controls on development near washes, mandating engineered drainage and bank stabilisation, and providing guidance on temporary solutions such as sandbags (Maricopa County, n.a).

6.5 Storm Risk Management

The Government of Mexico, through the National Water Commission (CONAGUA) and the National Coordination of Civil Protection (CNPC), urged authorities at all three levels of government and the general public to implement protection strategies. The National Meteorological Service forecasted heavy to torrential rain across five states, tidal waves reaching 5 to 6 metres in the Gulf of California

(Government of Mexico, 2026). Hydrological monitoring was kept at its highest level for the behaviour of rivers and streams, particularly those rivers with a rapid response time that can burst their banks within a few hours, as well as reservoir water levels (CONAGUA, 2026).

The Mexican government's emergency response units issued a warning for hurricane-force winds and implemented a series of preventive measures. These included community alerting campaigns, inspections of temporary shelters, clearance of drainage systems, and debris removal. Authorities also monitored flood-prone regions and water levels in rivers and reservoirs, while deploying emergency personnel and specialised equipment, and preparing shelters along with evacuation support. Nearly 6,900 federal, state, and military personnel were mobilized throughout Baja California Sur, with additional coordination and preparedness efforts in Sonora (Government of Mexico, 2026). A total of 554 temporary shelters were available, activated based on the population needs in Baja California Sur, Sonora, Chihuahua, and Sinaloa. Power and water supplies were cut in the three most exposed municipalities Comondú, Mulegé, and Loreto, as a safety measure (EFE, 2026). Further south, in the states of Jalisco, Michoacán, and Guerrero, schools and businesses closed, all navigation at sea was cancelled, and ports were shut. High tides triggered tourism warnings in coastal areas, prompting authorities to restrict beach access (Redacción N+, 2026).

In Guaymas, municipal authorities undertook preventive cleaning of arroyos and storm-drain infrastructure, while residents in the fishing community of Puerto San Carlos constructed earthen barriers to protect against coastal flooding (Ayuntamiento de Guaymas, 2026; AP, 2026). These measures demonstrate that risk reduction efforts are being implemented both at the municipal level, through the maintenance of drainage infrastructure, and at the community level, through locally organised protective actions. However, the failure of the retaining wall in San Carlos, which allowed seawater to inundate residential areas, illustrates the limits of local protection when faced with severe coastal hazards. Their effectiveness is constrained by the capacity of existing drainage systems to manage intense rainfall and runoff, and by the ability of locally constructed barriers to withstand coastal flooding. This underscores the importance of pairing local preparedness with longer-term investments in resilient infrastructure and broader risk reduction strategies.

6.6 Critical systems and services

Polo left behind property damage in the Baja Peninsula and Sonora, and flooding in coastal and low-lying areas. Landslides blocked roads at several points of the federal highway (EFE, 2026). Preliminary assessments indicated no deaths, with minor structural damage and road flooding reported (PAHO, 2026). Around 700 people were evacuated and returned home the following day (Rosete, 2026).

The small fishing town of Puerto San Carlos, was the worst-affected area after a retaining wall broke and seawater flooded several neighbourhoods. At least 100 people were evacuated and taken to a shelter (Redacción N+, 2026). Small, low-lying fishing communities often depend on limited defences and possess restricted resources for recovery, so a failure can quickly become a displacement event.

Prior rainfall events had already saturated soils across parts of the U.S. Southwest, increasing runoff and flood risk when moisture associated with Hurricane Polo moved into the region (AP, 2026). The scale of the wider flood threat was also reflected in southern Arizona, where the National Weather Service's Tucson office issued 246 flash flood warnings during the 2026 monsoon season, the highest annual total in its archive since 2002, with seven warnings covering parts of Pima County on 29 September, as Polo's remnants affected the region (de Leon, 2026). These conditions contributed to

concerns over the stability of the McLeod Dam in Doña Ana County, New Mexico. The Weather Service issued a flash flood emergency and county officials ordered evacuations along the Rio Grande. Pumps were brought in to relieve pressure downstream, while residents of the communities of Rincon, Salem and Garfield were told to seek higher ground (D'Ammassa 2026; Breen, 2026). County officials later reported the dam had suffered only a small piping failure that was mitigated, and the evacuation orders were lifted within a day (Raess, 2026).

The emergence of Tropical Storm Rachel shortly after Hurricane Polo illustrates how risk can evolve through the interaction of multiple hazards and the systems responding to them (Schuettler, Hill and Brown, 2026). Although the two storms affected different areas along Mexico's Pacific coast, their preparation and response requirements overlapped in time. While authorities were still conducting debris removal, road clearance and recovery activities following Polo, they were simultaneously required to monitor Rachel, assess new impacts and deploy additional emergency resources (Government of Mexico, 2026). This exemplifies that cascading risk is not necessarily dependent upon hazards impacting the same area, and rather, successive events can place additional stress on emergency response capacities, infrastructure, and institutional resources while recovery from a previous event is still underway.

When multiple weather systems occur within a short period, the demands on emergency management can overlap even when their impacts are geographically distinct. In the case of Polo and Rachel, authorities had to manage the impacts and recovery needs associated with Baja California Sur and Sonora while monitoring and preparing for Rachel's threats to other parts of Mexico. This overlap highlights the importance of assessing risk in light of both current environmental conditions and available response capacity, including the condition of dams and flood control infrastructure, rather than considering each hazard in isolation.

Hazard maps and warnings that focus solely on the projected landfall zone can overlook communities affected by heavy rain, storm surges, and flash floods located away from the storm's direct path. Risk communication and response strategies should encompass the entire storm footprint, including areas affected by moisture days later. Polo demonstrates that a hurricane weakening before landfall can still cause significant damage through rainfall, flooding, and infrastructure impact. Similarly, it highlights that communities directly hit by hurricane-force winds may experience less damage if warnings, preparations, shelters, and response efforts are effectively managed.

7 Conclusions

Overall, it is clear that the wind speeds and conditions leading to Hurricane Polo have increased due to climate change. In particular, high winds have become robustly more likely and intense due to global warming leading to favourable environmental conditions for more intense tropical cyclones in the eastern Pacific, with agreement found across two different attribution analyses. Such conditions have also been amplified this season by the rising El Niño, by a comparable degree to the influence of global warming. There is also evidence from the historical record that the region of northwestern Mexico is experiencing increasingly intense extreme rainfall in the tropical cyclone season from September-November, but we are unable to quantify this due to the challenge of simulating changes in extreme tropical cyclone-related extreme rainfall in the region.

Data availability

All time series used in the attribution analysis are available via the Climate Explorer.

References

All references are given as hyperlinks in the text.

Appendix

A.1 Data and Methods

A.1.1 Extreme rainfall probabilistic attribution

A.1.1.1 Observational data

In this study, we use several observational and reanalysis datasets to characterise the extreme rainfall that occurred along the path of Hurricane Polo and the wider season:

1. The European Centre for Medium-Range Weather Forecasts's 5th generation reanalysis product, ERA5, is a gridded dataset that combines historical observations into global estimates using advanced modelling and data assimilation systems (Hersbach et al., 2020). We use daily precipitation data from this product at a resolution of 0.5°×0.5° and 0.25°×0.25°, from the years 1950 to present. The re-analysis is available until the end of 20th September 2026. We extend the re-analysis data with the ECMWF analysis until 6th October.
2. We use CPC daily precipitation. This is the gridded product from NOAA PSL, Boulder, Colorado, USA known as the CPC Global Unified Daily Gridded data, available at 0.5° x 0.5° resolution, for the period 1979-present. Data are available from NOAA.
3. The Multi-Source Weighted-Ensemble Precipitation (MSWEP) v2.8 dataset (updated from Beck et al., 2019) is fully global, available at 3-hourly intervals and at 0.1° spatial resolution, available from 1979 to ~3 hours from real-time. This product combines gauge-, satellite-, and reanalysis-based data, including ERA5.
4. The rainfall product developed by the UC Santa Barbara Climate Hazards Group called "Climate Hazards Group InfraRed Precipitation with Station data" (CHIRPS; Funk et al. 2015). Daily data are available at 0.05° resolution, from 1981-31 August 2026. The product incorporates satellite imagery with in-situ station data.
5. Station data

To identify the track of Hurricane Polo, we use the International Best Track Archive for Climate Stewardship (IBTrACS) (Knapp et al., 2010; Gahtan et al., 2024), available from the NCEI website. IBTrACS merges Tropical Cyclone (TC) storm track datasets from agencies around the world to create a global, best track TC database.

As a measure of anthropogenic climate change we use the (low-pass filtered) global mean surface temperature (GMST), where GMST is taken from the National Aeronautics and Space Administration (NASA) Goddard Institute for Space Science (GISS) surface temperature analysis (GISTEMP, Hansen et al., 2010 and Lenssen et al. 2019).

As a measure of the El Niño - Southern Oscillation cycle (ENSO) we use the detrended Niño3.4 index. This is computed from NOAA's ERSST v.5 sea surface temperatures, by subtracting the mean tropical SST (20°S-20°N) from the mean SST over the Nino3.4 region (5°S-5°N, 170°W-120°W). This index is therefore adjusted to remove the linear trend associated with climate change as proposed in van Oldenborgh et al., 2021, but without rescaling each calendar month.

A.1.1.2 Model and experiment descriptions

We use 3 multi-model ensembles from climate modelling experiments using very different framings (Philip et al., 2020): Sea Surface temperature (SST) driven global circulation high resolution models, coupled global circulation models and regional climate models.

1. Coordinated Regional Climate Downscaling Experiment (CORDEX) - North America (CORDEX-NAM) data archive contains output from regional climate models (RCMs) run over a domain covering most of North America using boundary conditions from global climate model (GCM) simulations in the CMIP5 archive. These simulations run from 1950–2100 with a spatial resolution of 0.22°/25km or 0.44°/50km (Mearns et al., 2017), composed of historical simulations up to 2005, and extended to the year 2100 using the RCP8.5 scenario.

2. The FLOR (Vecchi et al., 2014) and AM2.5C360 (Yang et al., 2021, Chan et al., 2021) climate models are developed at Geophysical Fluid Dynamics Laboratory (GFDL). The FLOR model is an atmosphere-ocean coupled GCM with a resolution of 50 km for land and atmosphere and 1 degree for ocean and ice. Ten ensemble simulations from FLOR are analysed, which cover the period from 1860 to 2100 and include both the historical and RCP4.5 experiments driven by transient radiative forcings from CMIP5 (Taylor et al., 2012). AM2.5C360 is atmospheric GCM based on that in the FLOR model (Delworth et al., 2012, Vecchi et al., 2014) with a horizontal resolution of 25 km (and is referred to as 'AM2' throughout this text). Three ensemble simulations of the Atmospheric Model Intercomparison Project (AMIP) experiment (1871-2100) from each of the two models are analysed. Radiative forcings are using historical values over 1871-2014 and RCP4.5 values after that. Simulations are initialised from three different pre-industrial conditions but forced by the same SSTs from HadISST1 (Rayner et al., 2003) after groupwise adjustments (Chan et al., 2021) over 1871-2020. SSTs between 2021 and 2100 are using the FLOR RCP4.5 experiment 10-ensemble mean values after bias correction.

3. HighResMIP SST-forced model ensemble (Haarsma et al. 2016), the simulations for which span from 1950 to 2050. The SST and sea ice forcings for the period 1950-2014 are obtained from the 0.25° x 0.25° Hadley Centre Global Sea Ice and Sea Surface Temperature dataset that have undergone area-weighted regridding to match the climate model resolution. For the 'future' time period (2015-2050), SST/sea-ice data are derived from RCP8.5 (CMIP5) data, and combined with greenhouse gas forcings from SSP5-8.5 (CMIP6) simulations (see Section 3.3 of Haarsma et al. 2016 for further details).

A.1.1.3 Statistical methods

Methods for observational and model analysis and for model evaluation and synthesis are used according to the World Weather Attribution Protocol, described in Philip et al., (2020), with supporting details found in van Oldenborgh et al., (2021), Ciavarella et al., (2021), Otto et al., (2024) and here. The key steps, presented in sections 3-6, are: (3) trend estimation from observations; (4) model validation; (5) multi-method multi-model attribution; and (6) synthesis of the attribution statement.

In this report we analyse time series of September-November maximum rainfall within a region in NW Mexico (section 2) and September mean potential intensity in a region of the eastern pacific around the track of Hurricane Polo (section 3).

A nonstationary GEV and Gaussian distribution are used to model the precipitation and potential intensity, respectively. For precipitation, the distribution is assumed to scale exponentially with the covariates, with the dispersion (the ratio between the standard deviation and the mean) remaining constant over time; while for potential intensity, due to its strong link to ocean temperature, the distribution is assumed to shift linearly with the covariates, while the variance remains constant. For each time series we calculate the return period and intensity of the event under study for the 2026 GMST and for 1.4°C cooler GMST: this allows us to compare the climate of now and of the preindustrial past without human-caused warming (based on Forster et al., 2026), by calculating the probability ratio (PR; the factor-change in the event's probability) and change in intensity of the event.

In order to examine the effect of the ENSO phase on these indices alongside that of increasing GMST, we extend the nonstationary model to accommodate an additional covariate. All results quoted in section 3, as well as the observation-based results in section 2, are from statistical models including both covariates.

For precipitation, the variable of interest, X, is assumed to follow a GEV distribution in which the location and scale parameters vary with both GMST and ENSO:

$$X \sim GEV(\mu, \sigma, \xi \mid \mu_0, \sigma_0, \alpha, \beta, T, I),$$

where X denotes the variable of interest, rainy-season precipitation; T is the smoothed GMST; I is the detrended Niño3.4 index; μ_0, σ_0 and ξ are the location, scale and shape parameters of the nonstationary distribution; and α, β are the trends due to GMST and ENSO, respectively. As a result, the location and scale of the distribution have a different value in each year, determined by both the GMST and Niño3.4 states. Maximum likelihood estimation is used to estimate the model parameters, with

$$\mu = \mu_0 exp\left(\frac{\alpha T + \beta I}{\mu_o}\right) \qquad \text{and} \qquad \sigma = \sigma_0 exp\left(\frac{\alpha T + \beta I}{\mu_o}\right).$$

This formulation reflects the Clausius Clapeyron relation, which implies that precipitation scales exponentially with temperature (Trenberth et.al., 2003, O'Gorman and Schneider 2009), and so that precipitation will scale exponentially with the strength of the detrended Niño3.4 index. Under this model, the effects of GMST and the detrended Niño3.4 index are assumed to be independent of one another, so that the change in intensity due to GMST is unaffected by the change in intensity due to the ENSO phase. We note that this may not be the case in the real world, as the intensity and frequency of El Niño events may have been influenced by climate change (Cai et al., 2021); however, by using a detrended Niño3.4 index (see Section A.1.1.1) we aim to minimise the correlation between the two factors, and so do not expect the qualitative findings of this study to be affected by this simplifying assumption.

Estimation of return periods with multiple covariates

Extra care must be taken when reporting and interpreting return periods that depend on more than one covariate. Typically, WWA reports estimated return periods for the event of interest under current climatic conditions: that is, with the GMST fixed at the 2026 level. In this study, there are two covariates to consider: the GMST and ENSO. By fixing both the ENSO and the GMST at their 2026 levels, we can estimate the return period of the 2026 event in the current climate and in the current IOD state. Mathematically, this return period is written as

$$1 / P(X > x_{2026} \mid T = t_{2026}, D = d_{2026}),$$

where x_{2026} is the 2026 value of observed precipitation; t_{2026} denotes the 2026 GMST; and d_{2026} denotes the 2026 IOD. Altogether, the expression in brackets gives the probability that X will exceed x_{2026}, given that $T = t_{2026}$ and $D = d_{2026}$; inverting this probability gives us an expected return period, in years.

However, this return period only tells us the probability of experiencing a similar event under current IOD conditions and current warming levels. In order to understand how frequently such an event is actually likely to occur, we must account for the fact that the IOD is not often in the strongly positive phase observed in 2026. To do this, we evaluate the return period over all states of the IOD that have been recorded since 1980 (the period covered by the available gridded data products). This is done by first averaging the probability of exceeding x_{2026} over all recorded values of d_{2026} during this period, then inverting to obtain the return period:

$$1 / \sum_{y=1980}^{2026} P(X > x_{2026} \mid T = t_{2026}, D = d_y).$$

Defining the ENSO state in climate models

The multi-method multi-model attribution step of the WWA protocol involves estimating, for each climate model, the effective return level of a 1-in-*n*-year event under the current climate state, and estimating the expected change in likelihood and intensity of such an event after a specified change in the covariates. Because the smoothed GMST is generally monotonically increasing, the standard WWA approach is simply to take the model's 2026 GMST as a covariate and to estimate the expected magnitude of an *n*-year event. However, the factual climate in this study is defined by the 2026 GMST and by the mean of the detrended Niño3.4 index during the rainy season. During the attribution step, the detrended Niño3.4 index derived from the climate model is standardised so that the subset from 1979-2026 has mean 0 and variance 1; the 'factual' climate is then defined as having the model's 2026 GMST and the 2026 observed value of the detrended Niño3.4 index, standardised in the same way. This removes any potential biases in the results due to differences between the amplitude of the modelled Niño3.4 index and that observed.

Synthesis

For each event definition, we evaluate the influence of anthropogenic climate change on the events by calculating the probability ratio as well as the change in intensity using observations and climate models. Models which do not pass the evaluation described above are excluded from the analysis (see section A.3). The aim is to synthesise results from models that pass the evaluation along with the observations-based products, to give an overarching attribution statement. Tables of the results of this model fitting can be found in Appendix A3.

Figure 2.7 shows the changes in intensity and probability for the observations (blue) and models (red). Before combining them into a synthesised assessment, first, a representation error is added (in quadrature) to the observations, to account for the difference between observations-based datasets that cannot be explained by natural variability. This is shown in these figures as white boxes around the light blue bars. The dark blue bar shows the average over the observation-based products. Next, a term to account for intermodel spread is added (in quadrature) to the natural variability of the models. This is shown in the figures as white boxes around the light red bars. The dark red bar shows the model average, consisting of a weighted mean using the (uncorrelated) uncertainties due to natural variability plus the term representing intermodel spread (i.e., the inverse square of the white bars).

Observation-based products and models are combined into a single result in two ways. Firstly, we neglect common model uncertainties beyond the intermodel spread that is depicted by the model average, and compute the weighted average of models (dark red bar) and observations (dark blue bar): this is indicated by the magenta bar. As, due to common model uncertainties, model uncertainty can be larger than the intermodel spread, secondly, we also show the more conservative estimate of an unweighted, direct average of observations (dark blue bar) and models (dark red bar) contributing 50% each, indicated by the white box around the magenta bar in the synthesis figures.

A.1.2 Potential intensity probabilistic attribution

A.1.2.1 Observational data

ERA5 (Hersbach et al., 2020) is used to analyse the anthropogenic influence upon the conditions leading to Hurricane Polo. We use sea surface temperatures, sea level pressure, and specific humidity and atmospheric temperatures at all available pressure levels from this product. The Potential Intensity is calculated from these variables using the open-source PyPI package (Gilford, 2021).

A.1.2.2 Model and experiment descriptions

To estimate the influence of anthropogenic climate change upon the potential intensity in which Helene occurred, we use the CMIP6 multi-model ensemble. This consists of simulations from 11 participating models with varying resolutions. For more details on CMIP6, please see Eyring et al., (2016). For all simulations, the period 1850 to 2015 is based on historical simulations, while the SSP5-8.5 scenario is used for the remainder of the 21st century.

A.1.2.3 Statistical methods

The methods for attribution of the extreme indices detailed above are the same as set out in section 2.1.3 with a few minor changes. A nonstationary Gaussian distribution is used to model each of these

indices. The distribution is assumed to shift linearly with the covariates, while the variance remains constant. The variable of interest is assumed to follow a normal distribution in which the location parameter varies with GMST:

$$X \sim N(\mu, \sigma \mid \mu_0,\ \sigma_0, \alpha, \beta,\ T,\ I),$$

where X denotes the variable of interest, potential intensity; T is the smoothed GMST; I is the detrended Niño3.4 index; μ_0 and σ_0 are the location and scale parameters of the nonstationary distribution; and α, β are the trends due to GMST and ENSO, respectively. As a result, the location of the distribution has a different value in each year, determined by the GMST and ENSO states. Maximum likelihood estimation is used to estimate the model parameters, with

$$\mu = \mu_0 + \alpha T + \beta I \qquad \text{and} \qquad \sigma = \sigma_0.$$

All other statistical methods follow those described in section A.1.1.3.

A.2 Additional details

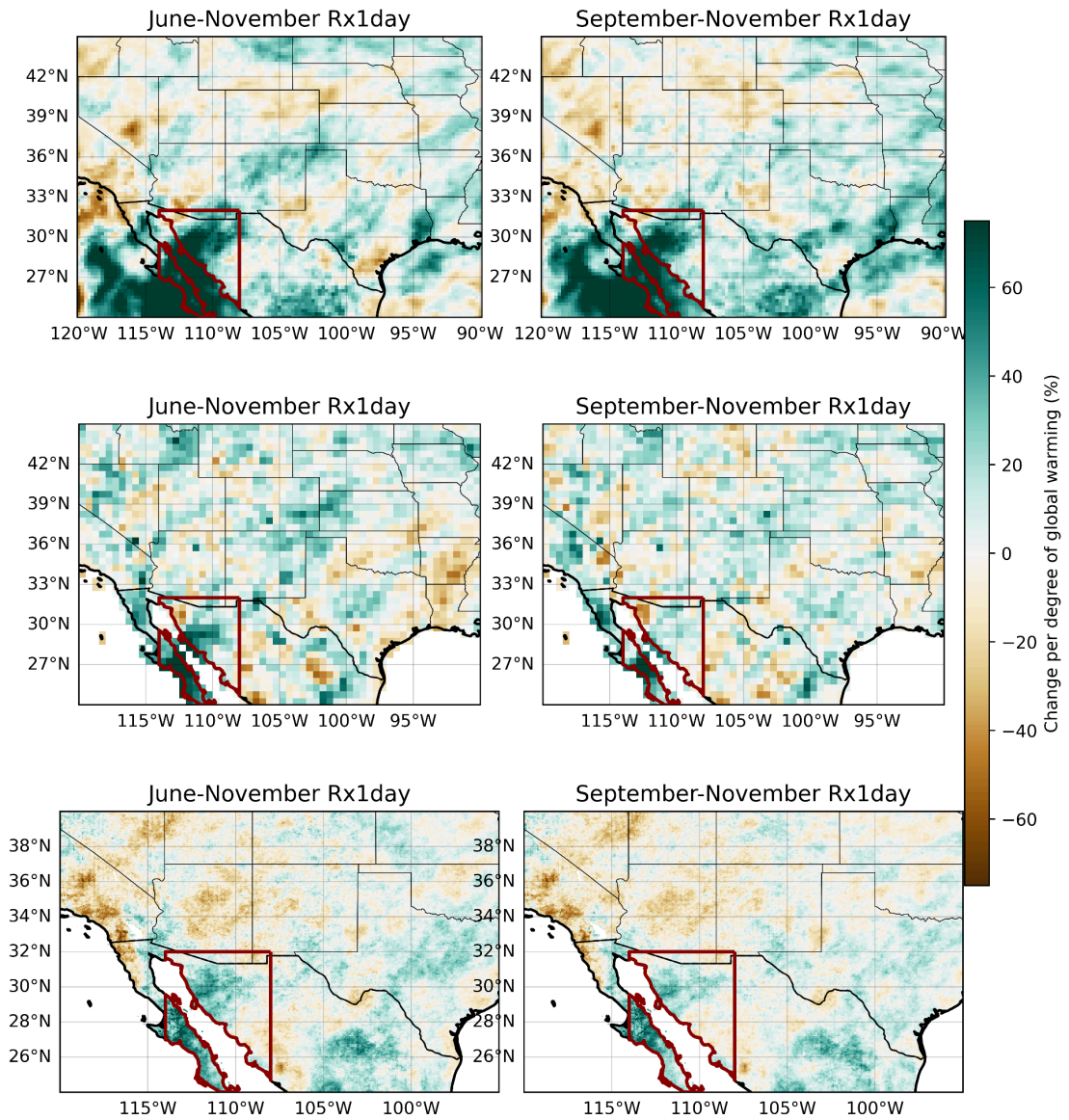

Figure A.2.1: *Linear trends in the wettest day of the June-November (left) and September-November (right) season in three observation-based datasets: ERA5, top; CPC, middle; CHIRPS, bottom. Trends are calculated with the relative precipitation at each grid cell, giving a fractional change at that location irrespective of the absolute totals. The study region is shown in dark red.*

A.3 Model evaluation tables

In the subsections below we show the results of the model evaluation for each location. For each framing or model setup we also use models that only just pass the evaluation tests if we only have five models or less for that framing that perform well. The tables show the model evaluation results.

In this section we show the results of the model evaluation for the assessed region. The climate models are evaluated against the observations in their ability to capture:

1. Seasonal cycles: For this, we qualitatively compare the seasonal cycles based on model outputs against observations-based cycles. We discard the models that exhibit ill-defined peaks in their seasonal cycles. We also discard the model if the rainy season onset/termination varies significantly from the observations.

2. Spatial patterns: Models that do not match the observations in terms of the large-scale precipitation and potential intensity patterns are excluded.

3. Parameters of the fitted statistical models: dispersion and shape for rainfall, sigma and the correlation with the relative Nino3.4 index for potential intensity. We discard the model if the model and observation parameters ranges do not overlap.

The models are labelled as 'good','reasonable', or 'bad' based on their performances in terms of the three criteria discussed above. A model is given an overall rating of 'good' if it is rated 'good' for all three characteristics. If there is at least one 'reasonable', then its overall rating will be 'reasonable' and 'bad' if there is at least one 'bad'.

Per framing or model setup we also use models that only just pass the validation tests if we only have five models or less for that framing that perform well. The tables show the model validation results.

A.3.1 Extreme rainfall model evaluation

Model / Observations	**Model run**	**Seasonal cycle**	**Spatial pattern**	**Dispersion**	**Shape parameter**	**Conclusion**
CHIRPS				0.336 (0.239 ... 0.419)	0.064 (-0.65 ... 0.63)	
CPC				0.349 (0.244 ... 0.417)	0.051 (-0.32 ... 0.64)	
ERA5				0.387 (0.315 ... 0.440)	-0.11 (-0.40 ... 0.034)	
CORDEX						
CCCma-CanESM2_CCCma-CanRCM4	r1i1p1	good	reasonable, bit too weak in southern mexico	0.515 (0.359 ... 0.603)	0.35 (0.025 ... 0.93)	reasonable
CCCma-CanESM2_OURANOS-CRCM5	r1i1p1	good, weak monsoon good tail	reasonable, bit too weak in southern mexico	0.663 (0.506 ... 0.768)	0.31 (0.072 ... 0.62)	bad
CCCma-CanESM2_SMHI-RCA4	r1i1p1	good, weak monsoon good tail	good	0.548 (0.415 ... 0.635)	0.55 (0.22 ... 0.95)	reasonable
CCCma-CanESM2_UQAM-CRCM5	r1i1p1	good, weak monsoon good tail	good	0.692 (0.541 ... 0.773)	0.39 (0.0060 ... 0.77)	bad

CNRM-CERFACS-CNRM-CM5_OURANOS-CRCM5	r1i1p1	good	good	0.561 (0.445 ... 0.643)	-0.070 (-0.36 ... 0.20)	bad
ICHEC-EC-EARTH_DMI-HIRHAM5_	r3i1p1	reasonable, monsoon start off but end is ok	good	0.459 (0.333 ... 0.539)	-0.10 (-0.38 ... 0.15)	reasonable
ICHEC-EC-EARTH_SMHI-RCA4	r12i1p1	reasonable, no clear monsoon end but could just be autumn storms	good	0.531 (0.411 ... 0.612)	-0.089 (-0.37 ... 0.10)	reasonable
MOHC-HadGEM2-ES_ISU-RegCM4	r1i1p1	good, monsoon too big but timing and tail good	reasonable, gulf rains too high	0.364 (0.280 ... 0.424)	-0.13 (-0.40 ... 0.093)	reasonable
MOHC-HadGEM2-ES_NCAR-WRF	r1i1p1	reasonable, monsoon end a little lengthy	good	0.446 (0.347 ... 0.516)	-0.037 (-0.25 ... 0.18)	reasonable
MPI-M-MPI-ESM-LR_GERICS-REMO2015	r1i1p1	bad, monsoon too long	reasonable, gulf rains too high	0.358 (0.270 ... 0.428)	-0.11 (-0.36 ... 0.077)	bad
MPI-M-MPI-ESM-LR_NCAR-RegCM4	r1i1p1	good	good	0.415 (0.296 ... 0.499)	-0.15 (-0.54 ... 0.059)	good
MPI-M-MPI-ESM-LR_OURANOS-CRCM5	r1i1p1	bad, monsoon too long	reasonable, southern rains too strong	0.362 (0.276 ... 0.406)	-0.20 (-0.51 ... 0.11)	bad
MPI-M-MPI-ESM-LR_UA-WRF	r1i1p1	good	good	0.404 (0.296 ... 0.489)	-0.12 (-0.34 ... 0.19)	good
MPI-M-MPI-ESM-LR_UQAM-CRCM5	r1i1p1	bad, monsoon too long	reasonable, southern rains too strong	0.360 (0.217 ... 0.432)	0.21 (-0.20 ... 0.88)	bad
MPI-M-MPI-ESM-MR_UQAM-CRCM5	r1i1p1	bad, monsoon timing and tail wrong	good	0.370 (0.294 ... 0.427)	-0.15 (-0.58 ... 0.20)	bad
NCC-NorESM1-M_GERICS-REMO2015	r1i1p1	bad, tail >> monsoon	good	0.399 (0.293 ... 0.480)	0.078 (-0.31 ... 0.39)	bad
NOAA-GFDL-GFDL-ESM2M_ISU-RegCM4	r1i1p1	reasonable, quite extreme tail	good	0.294 (0.223 ... 0.351)	-0.35 (-0.61 ... -0.082)	reasonable
NOAA-GFDL-GFDL-ESM2M_NCAR-WRF	r1i1p1	bad, monsoon and tail wrong	good	0.367 (0.267 ... 0.444)	-0.30 (-0.58 ... -0.12)	bad
NOAA-GFDL-GFDL-ESM2M_OURANOS-CRCM5	r1i1p1	bad, monsoon and tail wrong	good	0.284 (0.209 ... 0.334)	-0.12 (-0.52 ... 0.021)	bad
HighResMIP						
CMCC-CM2-HR4	r1i1p1f1	good	bad, too coarse	0.606 (0.459 ... 0.698)	0.26 (-0.16 ... 0.60)	bad
CMCC-CM2-VHR4	r1i1p1f1	good	good	0.595 (0.455 ... 0.689)	0.28 (-0.0099 ... 0.64)	bad
CNRM-CM6-1-HR	r1i1p1f2	bad, no monsoon	good	0.591 (0.451 ...	0.015 (-0.35 ...	bad

				0.705)	0.22)	
CNRM-CM6-1	r1i1p1f2	bad, no monsoon	bad, too coarse	0.735 (0.594 ... 0.861)	-0.040 (-0.54 ... 0.31)	bad
EC-Earth3P-HR	r1i1p1f1	good	good	0.510 (0.405 ... 0.580)	0.39 (0.13 ... 0.85)	reasonable
EC-Earth3P-HR	r2i1p1f1	good	good	0.506 (0.377 ... 0.593)	0.35 (0.12 ... 0.60)	reasonable
EC-Earth3P-HR	r3i1p1f1	good	good	0.470 (0.369 ... 0.535)	0.14 (-0.30 ... 0.44)	reasonable
EC-Earth3P	r1i1p1f1	good	bad, too coarse	0.460 (0.351 ... 0.522)	0.24 (-0.027 ... 0.68)	bad
EC-Earth3P	r2i1p1f1	good	bad, too coarse	0.548 (0.407 ... 0.641)	0.32 (0.020 ... 0.61)	bad
EC-Earth3P	r3i1p1f1	good	bad, too coarse	0.508 (0.363 ... 0.624)	-0.038 (-0.42 ... 0.12)	bad
HadGEM3-GC31-HM	r1i1p1f1	good	good	0.504 (0.386 ... 0.588)	-0.072 (-0.29 ... 0.12)	reasonable
HadGEM3-GC31-HM	r1i2p1f1	good	good	0.458 (0.317 ... 0.539)	0.050 (-0.20 ... 0.33)	reasonable
HadGEM3-GC31-HM	r1i3p1f1	good	good	0.494 (0.371 ... 0.577)	-0.22 (-0.62 ... 0.29)	reasonable
HadGEM3-GC31-LM	r1i14p1f1	good	bad, too coarse	0.637 (0.473 ... 0.749)	0.22 (0.029 ... 0.60)	bad
HadGEM3-GC31-LM	r1i15p1f1	good	bad, too coarse	0.527 (0.392 ... 0.599)	0.27 (-0.16 ... 0.82)	bad
HadGEM3-GC31-LM	r1i1p1f1	good	bad, too coarse	0.557 (0.428 ... 0.625)	0.32 (-0.24 ... 0.95)	bad
HadGEM3-GC31-LM	r1i2p1f1	good	bad, too coarse	0.539 (0.409 ... 0.626)	0.29 (-0.023 ... 0.57)	bad
HadGEM3-GC31-LM	r1i3p1f1	good	bad, too coarse	0.494 (0.399 ... 0.557)	-0.070 (-0.29 ... 0.26)	bad
HadGEM3-GC31-MM	r1i1p1f1	good	bad, too coarse	0.484 (0.379 ... 0.554)	0.14 (-0.26 ... 0.52)	bad
HadGEM3-GC31-MM	r1i2p1f1	good	bad, too coarse	0.599 (0.459 ... 0.701)	0.12 (-0.27 ... 0.34)	bad
HadGEM3-GC31-MM	r1i3p1f1	good	bad, too coarse	0.469 (0.340 ... 0.556)	-0.022 (-0.27 ... 0.25)	bad
MPI-ESM1-2-HR	r1i1p1f1	reasonable, monsoon start off but end is ok	bad, too coarse	0.658 (0.524 ... 0.738)	0.47 (-0.14 ... 0.85)	bad
MPI-ESM1-2-XR	r1i1p1f1	good	good	0.495 (0.383 ... 0.583)	0.32 (-0.039 ... 0.66)	reasonable
FLOR (Findings consistent across ensemble members)	Member 10 of 10	reasonable, monsoon no distinct but autumn tail clear	good	0.448 (0.344 ... 0.527)	-0.030 (-0.34 ... 0.18)	reasonable

AM2.5C360 (Findings consistent across ensemble members)	Member 1 of 3	good, monsoon distinct and autumn extremes represented	good	0.653 (0.503 ... 0.762)	0.049 (-0.45 ... 0.36)	bad

Table A.3.1 Evaluation results of the climate models considered for attribution analysis of Rx1dayTC. For each model, the best estimates of the Dispersion and Shape parameters are shown, along with 95% confidence intervals. Furthermore, evaluation of the seasonal cycle and spatial pattern are shown.

A.3.2 Potential intensity model evaluation

Of the 22 CMIP6 models analysed, 12 were rated 'bad' and discarded from the attribution analysis. No models performed well across all criteria, so all 10 remaining models were used.

Model / Observations	**Seasonal cycle**	**Spatial pattern**	**Sigma**	**Shape parameter**	**Conclusion**
ERA5			2.78 (2.29 ... 3.17)	0.46 (0.27 ... 0.61)	
CMIP6					
ACCESS-CM2_r1i1p1f1	good	good	5.66 (4.43 ... 6.48)	0.30 (0.17 ... 0.43)	bad
BCC-CSM2-MR_r1i1p1f1	reasonable	reasonable	3.88 (2.93 ... 4.56)	0.33 (0.21 ... 0.44)	reasonable
CanESM5_r1i1p1f1	reasonable	reasonable	3.53 (2.86 ... 3.96)	0.48 (0.38 ... 0.58)	reasonable
CanESM5-CanOE_r1i1p2f1	reasonable	reasonable	4.06 (3.16 ... 4.68)	0.47 (0.37 ... 0.57)	reasonable
CESM2_r4i1p1f1	reasonable	reasonable	3.65 (2.68 ... 4.28)	0.54 (0.44 ... 0.63)	reasonable
CESM2-WACCM_r1i1p1f1	reasonable	reasonable	3.76 (2.86 ... 4.41)	0.60 (0.51 ... 0.67)	reasonable
CIESM_r1i1p1f1	reasonable	reasonable	3.54 (2.66 ... 4.13)	0.46 (0.37 ... 0.57)	reasonable
CMCC-CM2-SR5_r1i1p1f1	reasonable	reasonable	1.56 (1.16 ... 1.83)	0.47 (0.36 ... 0.57)	bad
CMCC-ESM2_r1i1p1f1	reasonable	reasonable	1.90 (1.47 ... 2.20)	0.49 (0.39 ... 0.59)	bad
CNRM-CM6-1_r1i1p1f2	reasonable	bad	3.12 (2.40 ... 3.64)	0.22 (0.074 ... 0.35)	bad
CNRM-ESM2-1_r1i1p1f2	reasonable	bad	2.80 (2.16 ... 3.25)	0.28 (0.14 ... 0.41)	bad
EC-Earth3-CC_r1i1p1f1	reasonable	reasonable	3.24 (2.47 ... 3.69)	0.26 (0.13 ... 0.38)	reasonable
EC-Earth3-Veg-LR_r1i1p1f1	reasonable	reasonable	3.20 (2.50 ... 3.71)	0.24 (0.098 ... 0.39)	reasonable
FGOALS-f3-L_r1i1p1f1	reasonable	bad	2.84 (2.15 ... 3.24)	0.27 (0.14 ... 0.39)	bad
GFDL-ESM4_r1i1p1f1	reasonable	good	2.53 (1.94 ... 2.93)	0.49 (0.41 ... 0.57)	reasonable
HadGEM3-GC31-LL_r1i1p1f3	reasonable	reasonable	5.08 (3.85 ... 5.91)	0.35 (0.24 ... 0.47)	bad
KACE-1-0-G_r1i1p1f1	bad	bad	3.45 (2.61 ... 4.03)	-0.25 (-0.37 ... -0.12)	bad
MIROC6_r1i1p1f1	reasonable	reasonable	4.82 (3.66 ... 5.60)	0.54 (0.44 ... 0.62)	bad
MPI-ESM1-2-LR_r1i1p1f1	bad	reasonable	4.34 (3.45 ... 4.93)	0.53 (0.42 ... 0.61)	bad
MRI-ESM2-0_r1i1p1f1	reasonable	reasonable	3.91 (3.03 ... 4.44)	0.42 (0.32 ... 0.52)	reasonable

NESM3_r1i1p1f1	bad	bad	3.69 (2.91 ... 4.21)	0.33 (0.22 ... 0.43)	bad
NorESM2-LM_r1i1p1f1	reasonable	reasonable	4.64 (3.40 ... 5.60)	0.59 (0.51 ... 0.67)	bad

Table A.3.2: *Evaluation of the climate models considered for attribution of potential intensity around the track of Hurricane Polo. For each model, the best estimate of the sigma parameter and correlation with the relative Nino3.4 is shown with a 95% confidence interval, obtained via bootstrapping. The qualitative evaluation is shown in the right-hand column.*